Applied Energy 237 (2019) 519–533

Contents lists available at ScienceDirect

Applied Energy

journal homepage: www.elsevier.com/locate/apenergy

A New Three-point-based Approach for the Parameter Extraction of Photovoltaic Cells

Vun Jack Chin, Zainal Salam*

Centre of Electrical Energy Systems, School of Electrical Engineering, Universiti Teknologi Malaysia, Johor Bahru 81310, Malaysia
Institute of Future Energy, Universiti Teknologi Malaysia, Johor Bahru 81310, Malaysia

HIGHLIGHTS

- A novel three-point-based parameter extraction method is introduced.
- The method is substantially more accurate compared to other relevant works.
- Moreover, it locates the optimal solution within very low number of iterations.
- The statistics over 35 runs indicate exceptionally consistent results.

ARTICLE INFO

Keywords:
Solar photovoltaic
Parameter extraction
Equivalent circuit model
Pivot points
Evolutionary algorithm

ABSTRACT

This paper proposes a novel three-point based parameter extraction method for the single diode model. Unlike conventional curve-fitting procedures, the solution is simplistic yet exhibits outstanding ability to locate highly accurate solutions within very low number of iterations. The main idea is to establish three geometrically critical data points as the pivot points. By forcing the model to pass though these points exactly, the evolutionary algorithm (in this case differential evolution) is only utilized to fine-tune the remaining sections of the curve for best fit. As a result, the complexity of the algorithm is greatly reduced. A set of comparisons based on four case studies indicates that the proposed method substantially more accurate than other documented methods. Additionally, other tests with different types of photovoltaic modules (i.e. monocrystalline, polycrystalline, and thin film) at varying environmental conditions prove that the algorithm is reliable and practical for real-world applications. Besides, the scheme is highly efficient—it converges to the optimal solution in less than 50 iterations. Moreover, the solutions obtained are exceptionally consistent, i.e. the standard deviation of the root-mean-square error over 35 runs is at least 4 orders of magnitude less than those reported in other works. With these merits, the proposed method is envisaged to be valuable for both offline analysis and online monitoring applications where an accurate, fast and consistent parameter extraction tool is required.

1. Introduction

The depletion of fossil fuels reserves, the growing public awareness on global warming and the ever-rising energy demand have positioned mankind in the search of renewable energy sources (RES) that are clean, economical, and sustainable [1,2]. Among the RES available today, solar photovoltaic (PV) is considered one of the most promising, due to several important advantages: (1) ease of installation, (2) almost maintenance free, (3) highly scalable and (4) does not emit greenhouse gases or noise during normal operation. These factors, along with the development of increasingly cheaper and more efficient solar cells [3,4], have led to an astonishing growth in the production of cells and installation of PV systems [5,6]. In 2017 alone, at least 98 GW of solar PV capacity were installed globally—this brings the cumulative total to over 400 GW, almost a two-fold increase from 2015 [7].

The three major types of PV cells in use today are monocrystalline, polycrystalline and thin film: both crystalline technologies occupy more than 90% of the cells produced throughout the world [8], while the thin film accounts for approximately 4.5% [9]. Since these cells are silicon-based, their characteristics can be determined using the electrical-based diode models [10–12]. These are lumped parameter models, in which each circuit component (known as model parameter) correlates to a specific physical mechanism that occur within the solar cell. For instance, the series resistance represents the ohmic losses due to bulk resistance of the semiconductor material and metallic contacts; while the shunt

* Corresponding author at: Centre of Electrical Energy Systems, School of Electrical Engineering, Universiti Teknologi Malaysia, Johor Bahru 81310, Malaysia; Institute of Future Energy, Universiti Teknologi Malaysia, Johor Bahru 81310, Malaysia.
E-mail address: zainals@fke.utm.my (Z. Salam).

https://doi.org/10.1016/j.apenergy.2019.01.009
Received 23 August 2018; Received in revised form 12 December 2018; Accepted 1 January 2019
Available online 11 January 2019

resistance accounts for the leakage current in the *p-n* junction. There are also other emerging cells such as organic [13–15] and multi-junction [16]. However, due to their distinctively different structure, they require specialized models—which are beyond the scope of this work.

The precise knowledge of the model parameters values is crucial for many practical applications. For example, they are used in the simulation and emulation of PV systems [17–19], which are imperative for energy yield prediction and the characterization of power converter hardware. Further, these parameters are valuable for the quality control of PV cell during the manufacturing process [20]. Another area where these parameters are useful is in the study of the PV cell degradation [21–24]. However, the values of these parameters are not readily available in the manufacturer datasheet. Moreover, while the cell/module specifications (such as peak rated maximum power, short-circuit current and open-circuit voltage) are normally given at standard test conditions (STC),[1] the actual PV systems operate at conditions far from the ideal. Aside from the operating conditions, the model parameters vary from one module to another depending on the age, materials, and the adopted manufacturing technique [24–26].

The model parameters are normally determined in two ways. First is the analytical approach. It utilizes information on several key points on the *I-V* curve, i.e. open circuit voltage, short circuit current, maximum power voltage and maximum power current, and the slopes of the curve at the axes intersections. Despite its simplicity and rapid computations, the assumptions used in the approach often lead to inaccurate and physically unrealistic values [17,27,28]. Moreover, since the parameters are derived based on only few selected points, the solutions are more susceptible to measurement noise [29]. The second is the numerical extraction approach. It is basically an optimization process that minimizes the error between the computed *I-V* curve and experimental dataset. The latter may be collected from monitoring hardware/sensors or extracted from the manufacturer datasheet [10,17,29–32]. This approach is substantially more accurate than its analytical counterpart [17,33]. On the optimization algorithm itself, it can be divided into two categories: deterministic and stochastic. Deterministic methods are usually gradient-based, for instance, the Newton-Raphson method [34], iterative curve-fitting [35], conductivity method [36] and Levenberg–Marquardt algorithm [22,37]. Despite their effectiveness in local search, they inherit several limitations: they require continuity, convexity and differentiability of the objective function. It is recognized that, an inappropriate choice of initial conditions may lead to non-convergence. Also, as the number of parameters increases, the optimizer loses its ability to produce accurate results [38,39].

To overcome these drawbacks, stochastic optimization techniques such as evolutionary algorithms (EAs) are employed for the parameter extraction problem. These methods include genetic algorithm (GA) [19,20,40,41], particle swarm optimization (PSO) [31,42–45], differential evolution (DE) [27,46,47], simulated annealing (SA) [39], cuckoo search (CS) [48], harmony search (HS) [49], pattern search (PS) [50,51], artificial bee swarm optimization (ABSO) [52], the bird mating optimizer (BMO) [53], artificial bee colony (ABC) [54,55], and chaotic whale optimizer algorithm (CWOA) [10]. They are particularly attractive due to their global search capability, and their effectiveness in handling nonlinear functions without gradient information. Furthermore, the solutions do not depend on the choice of the initial conditions. The EAs have been proven to be superior in terms of accuracy and robustness compared to the deterministic algorithms [42,49,51]. However, the existing methods directly employ EA to optimize all model parameters—which inevitably lead to a solution search space with large number of dimensions. Due to the sheer number of candidate solutions that the optimizer has to evaluate prior to approaching a good-quality fit, these algorithms are time-consuming and prone to consistency issues; typically, few thousands of iterations are required to achieve satisfactory solutions [10,42,53,55–58]. Additionally, depending on the complexity of the search surface, the algorithms tend to get trapped in local optimal solutions [52,59].

In this paper, a new three-point-based parameter extraction method is proposed for the single diode model. The single diode model is chosen for its excellent compromise between simplicity and accuracy [60]. Numerous works have shown that, when properly optimized, it can offer comparable accuracy to the two-diode model [32,57,59]. This is despite the fact that the latter comprises more unknown parameters. Unlike the conventional curve-fitting approach, the proposed method extracts the model parameters in a two-phase process. First, three *pivot points* are chosen from the experimental dataset. These points are selected to be close to the geometrically critical regions of the *I-V* curve. By forcing the curve to pass through these points exactly, the explicit expressions of I_{PV}, I_o and R_p as functions of a and R_s can be derived. Consequently, the five unknown parameters in the model are reduced to two. During the second phase of the algorithm, the EA is utilized to adjust only the remaining sections of the curve in order to achieve best fit. This can be achieved easily by fine-tuning the values of a and R_s. With the combination of these two mechanisms, the complexity of the optimization is greatly reduced. Furthermore, to ensure physically meaningful results, several parametric constraints are introduced to eliminate out-of-bounds vectors during the optimization process.

Despite the simplistic nature of the scheme, it contributes to substantial improvement in terms speed, without compromising the accuracy. In addition, unlike the conventional EA methods that need to optimize five variables (of the single diode model), the proposed scheme exhibits remarkable consistency because the decision variables are now reduced to two. Furthermore, it does not require any additional information, except the experimental *I-V* data points and knowledge on the PV cell configuration (for PV module). Another important point to note is that, the method does not rely on approximation or simplification of the PV model.

In this work, DE is chosen as the optimization tool due to its outstanding global search capability, rapid convergence and few control parameters [27,61]. Nonetheless, the application of the proposed work is not limited to DE; other algorithms may also be used. For validation, the proposed method is employed to extract the model parameters for four experimental datasets of actual PV cells [34,62], namely: (1) 57 mm silicon solar cell from R.T.C France; (2) Schutten Solar STM6-40/36 monocrystalline module; (3) Schutten STP6-120/36 polycrystalline module; and (4) Photowatt-PWP 201 polycrystalline module. The results are compared against other well-established parameter extraction algorithms in the literature. In addition, the algorithm is tested on three other PV modules of different types (monocrystalline, polycrystalline and thin film) at varying levels of irradiance and temperature. The results indicate that the proposed method is substantially more accurate than other documented parameter extraction methods. Besides, the algorithm is highly efficient, i.e. it consistently converges to the optimal solution within a very low number of iterations (less than 50 iterations).

The remainder of the paper is organized as follows: Section 2 presents the basics of the single diode model; Section 3 briefly explains the concept of the DE algorithm; Section 4 defines parameter extraction problem and introduces the proposed algorithm; Section 5 analyzes and compares the performance of the proposed method with other methods using three case studies. Lastly, Section 6 concludes the paper.

2. The single diode model

A PV cell can be regarded as a silicon diode, with its *p-n* junction exposed to the environment [60,63]. The output of several PV cells connected in series and/or parallel can be described using the single diode model, as shown in Fig. 1. According to Kirchhoff's current law and Shockley diode equation, the *I-V* relationship of the model is defined as:

$$I = I_{PV}N_p - I_oN_p\left(e^{\frac{V+IR_s(N_s/N_p)}{aV_t}} - 1\right) - \frac{V + IR_s(N_s/N_p)}{R_p(N_s/N_p)} \quad (1)$$

[1] STC corresponds to solar irradiance of 1000 W/m^2 with 1.5 air mass spectral distribution at temperature 25 °C.

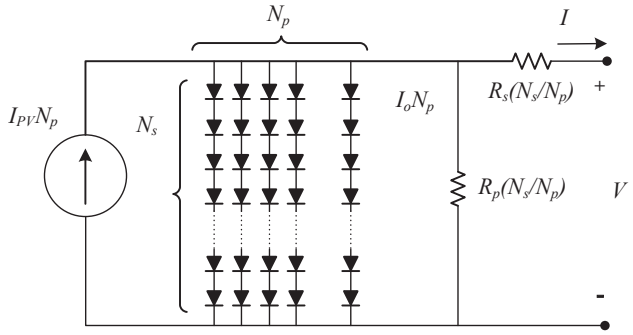

Fig. 1. Topology of the single diode model for $N_s \times N_p$ connection of solar cells.

where N_p and N_s are the number of PV cells in parallel and series, respectively. I_{PV} is the photocurrent and a represents the diode ideality factor. $V_t = N_s kT/q$ is the thermal voltage of the module. k is the Boltzman constant ($1.3806503 \times 10^{-23}$ J/K), T is the temperature in Kelvin, and q is the electron charge $1.60217646 \times 10^{-19}$ C). R_s and R_p are the series and shunt resistance, respectively. In total, the model is characterized by five unknown parameters, i.e., I_{PV}, I_o, a, R_s, and R_p.

3. Differential evolution

DE is a powerful stochastic real-valued parameter optimization algorithm introduced by Storn and Price in 1995 [64,65]. Similar to genetic algorithm (GA), the working principle of DE is inspired by the Darwinian theory of natural selection and genetics reproduction. However, instead of relying on the crossover operation, DE employs mutation operation (i.e. difference vectors) as the key mechanism to explore prospective regions of the search space. Like other members of the EA family, the DE algorithm begins with a population of randomly generated candidate solutions. Next, the solutions are iteratively improved through generations of mutation, crossover and selection operations, based on an appropriate objective function. The processes are reiterated until a stopping criterion is met—usually a predefined fitness value threshold, i.e. value-to-reach (VTR), or a maximum number of generations (Gen_{max}). Fig. 2 shows an overview of the DE optimization process in the form of operational block diagrams.

A. Initialization

In the initialization operation, a population of NP D-dimensional real-valued candidate solutions is created in the form of *target* vectors: $X_{i,Gen} = [X_{1,i,Gen}, X_{2,i,Gen},..., X_{j,i,Gen},..., X_{D,i,Gen}]$; where i denotes the population index ($i = 1, 2, ..., NP$), D is the number of decision variables, and Gen indicates the generation index. These vectors are generated by random within a user-defined search boundary, i.e.

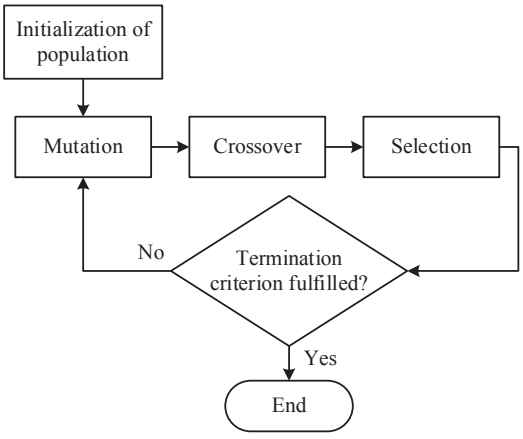

Fig. 2. Main operations of the DE algorithm.

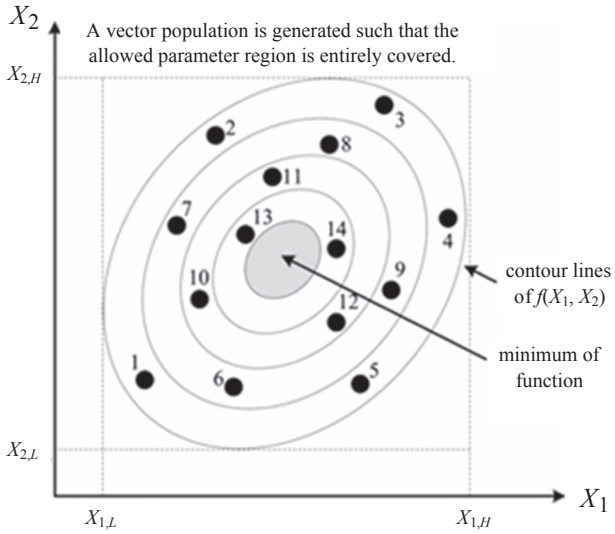

Fig. 3. Initialization operation of DE in a 2-dimensional search space.

$$X_{j,i,Gen} = X_L + rand[0, 1](X_H - X_L) \quad (2)$$

where $X_L = [X_{1,L}, X_{2,L},..., X_{D,L}]$ and $X_H = [X_{1,H}, X_{2,H},..., X_{D,H}]$ are the lower and upper bound of the search space, respectively. rand[0,1] is a randomly generated number between 0 and 1, following a uniform distribution. Fig. 3 illustrates the initialization operation of DE in a 2-dimensional search space.

B. Mutation

For every target vector, a *donor* vector is created by adding the weighted difference between two randomly chosen target vectors ($X_{r2,Gen}$ and $X_{r3,Gen}$) to a *base* vector ($X_{r1,Gen}$), given by,

$$V_{i,Gen} = X_{best,Gen} + F(X_{r1,Gen} - X_{r2,Gen}) \quad (3)$$

where $r1$ and $r2$ are randomly selected population indices, that are distinct to one another (i.e. $r1 \neq r2 \neq i$). $X_{best,Gen}$ is the vector with the best fitness value (i.e., lowest for a minimization problem) at the current generation. F denotes the mutation scaling factor; its value is normally chosen within the range [0, 1]. Fig. 4 depicts the mutation operation in a 2-dimensional parameter space (with constant cost contours of an arbitrary objective function).

C. Crossover

A crossover operator is employed to generate a population *trial* vectors ($U_{j,i,Gen}$), using elements selected from both $X_{j,i,Gen}$ and $V_{j,i,Gen}$, as shown in Eq. (4). There are two types of crossover strategies, namely, exponential and binomial crossover. In this work, the latter is utilized, i.e.

$$U_{j,i,Gen} = \begin{cases} V_{j,i,Gen}, & \text{if } (rand \leqslant CR \text{ or } j = j_{rand}) \\ X_{j,i,Gen}, & \text{otherwise} \end{cases} \quad (4)$$

where $j_{rand} \in [1, 2..., D]$ is a random variable index. It guarantees that at least one element of $U_{i,Gen}$ is taken from $V_{i,Gen}$. Fig. 5 shows the possible trial vectors $U_{i,Gen}$ from uniformly crossing $V_{i,Gen}$ and $X_{i,Gen}$.

One problem with the conventional DE is that non-physical solutions may be obtained as a result of the mutation operation. To prevent such occurrence, a simple penalty function is imposed [29]. By this function, any element that violates the predefined search boundaries is reinitialized using the operator defined in Eq. (5).

Fig. 6 depicts the effects of the penalty function in a 2-D parameter space.

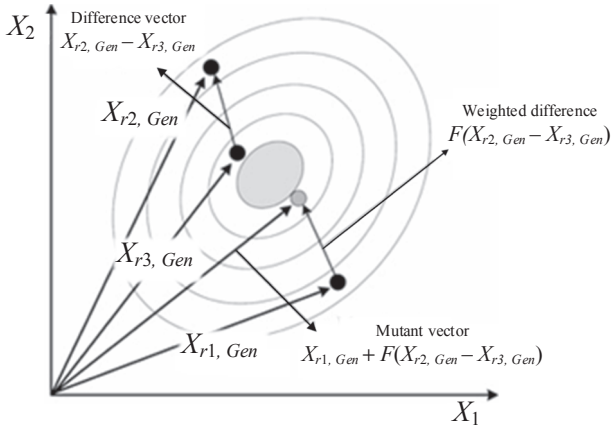

Fig. 4. Mutation operation of DE.

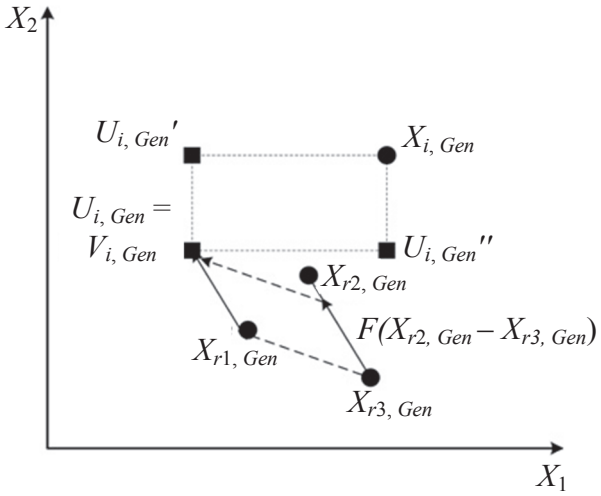

Fig. 5. Crossover operation of DE.

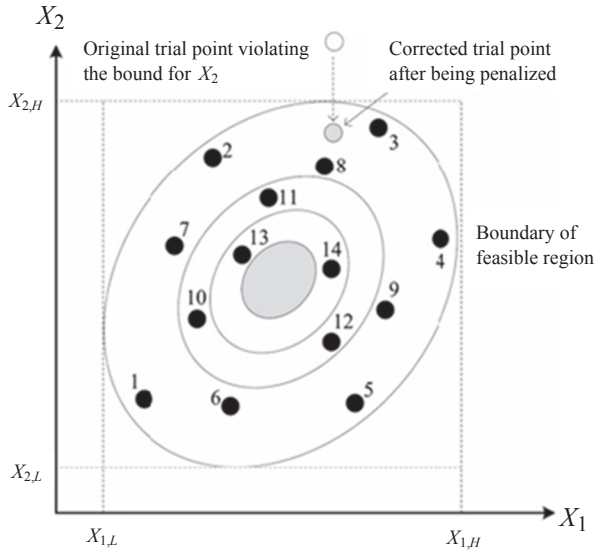

Fig. 6. Effects of penalty function.

$$U_{i,Gen+1} = \begin{cases} U_{i,Gen+1} - rand\,[0,\,1](X_H - X_L), & \text{if } U_{i,Gen+1} > X_{iH} \\ U_{i,Gen+1} + rand\,[0,\,1](X_H - X_L), & \text{if } U_{i,Gen+1} < X_{iL} \end{cases} \quad (5)$$

D. Selection

Step 1
Setting DE control parameters:
Maximum generation Gen_{max}, population size NP,
crossover rate CR, mutation factor F and
search ranges of the decision parameters.

Step 2
Set $Gen = 1$
Initialize a population of NP individuals, with
$X_{i,Gen} = [X_{1,i,Gen}, X_{2,i,Gen}, .., X_{j,i,Gen}, .., X_{D,i,Gen}]$
uniformly distributed in the range $[X_L, X_H]$ as:
$X_{j,i,0} = X_L + rand[0,1](X_H - X_L)$ where
$X_L = [X_{1,L}, X_{2,L}, \ldots, X_{D,L}]$ and
$X_H = [X_{1,H}, X_{2,H}, \ldots, X_{D,H}]$ with $i = [1, 2, \ldots, NP]$

Step 3
WHILE $Gen \le Gen_{max}$
DO
FOR $i = 1$ to NP

Step 3.1 Mutation Step
Generate a donor vector
$V_{i,Gen} = [V_{1,i,Gen}, V_{2,i,Gen}, .., V_{j,i,Gen}, .., V_{D,i,Gen}]$
Corresponding to the i^{th} target vector $X_{i,Gen}$ using
the differential evolution scheme of DE as:
$V_{i,Gen} = X_{r1,\,Gen} + F(X_{r2,\,Gen} - X_{r3,\,Gen})$

Step 3.2 Crossover Step
Generate a trial vector
$U_{i,Gen} = [U_{1,i,Gen}, U_{2,i,Gen}, .., U_{j,i,Gen}, .., U_{D,i,Gen}]$
for the i^{th} target vector $X_{i,Gen}$ using binomial
crossover in the following way:
$U_{i,\,j,\,Gen} = V_{i,\,j,\,Gen}$, if $(rand_{i,j}[0,\,1] \le CR$ or $j = j_{rand})$
$X_{i,\,j,\,Gen}$, otherwise.

Step 3.2.1 Penalty Function
IF $U_{j,i,Gen} < X_L$, THEN $U_{j,i,Gen} = X_L - rand_{i,j}[0,\,1](X_H - X_L)$
ELSEIF $U_{j,i,Gen} > X_H$, THEN $U_{j,i,Gen} = X_H - rand_{i,j}[0,\,1](X_H - X_L)$
END IF

Step 3.3 Selection and Evaluation Step
Evaluate the trial vector $U_{i,Gen}$
IF $J(U_{i,\,Gen}) < J(X_{i,Gen})$, THEN $X_{i,\,Gen+1} = U_{i,\,Gen}$
ELSE $X_{i,\,j,\,Gen+1} = X_{i,\,j,\,Gen}$
END IF
END FOR

Step 3.4 Increment of the Generation Count
$Gen = Gen + 1$
END WHILE

Fig. 7. Pseudo-code of the DE algorithm.

A tournament selection scheme is employed to select the vectors for the subsequent generation ($Gen = Gen + 1$), i.e.

$$X_{i,Gen} = \begin{cases} U_{i,Gen}, & \text{if } J(U_{i,Gen}) < J(X_{i,Gen}) \\ X_{i,Gen}, & \text{otherwise} \end{cases} \quad (6)$$

where $J(X)$ is the objective function to be minimized. If $U_{i,Gen}$ yields lower fitness value than its corresponding target vector $X_{i,Gen}$, the latter will be replaced by $U_{i,Gen}$. Otherwise, $X_{i,Gen}$ will be retained in the following generation. Therefore, the global fitness of the population will either improve or remain the same with each succeeding generation, but never deteriorate. The pseudo-code of the DE algorithm is presented in Fig. 7.

4. Problem formulation

As discussed in Section 2, the main objective of the parameter extraction problem is to identify the set of model parameters values which accurately describe the output of an actual PV cell/module. This task

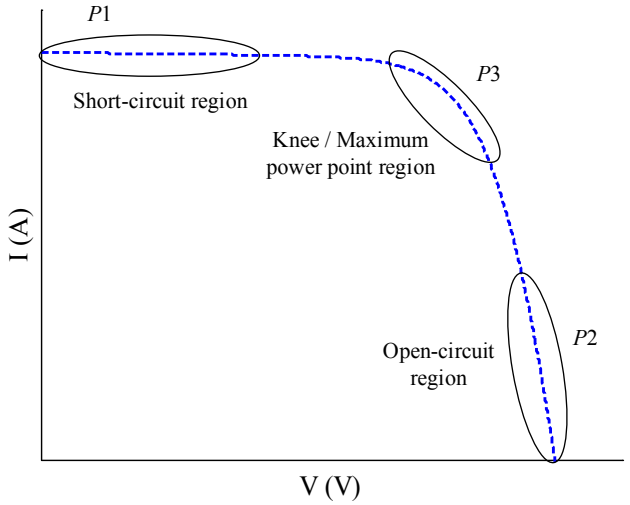

Fig. 8. Critical points of the *I-V* curve.

can be interpreted as an optimization problem, in which the objective is to minimize the point-by-point difference between computed *I-V* curve and the experimental dataset. The most widely accepted method to quantify such error is to utilize the root mean squared error (RMSE) [10,19,39,59,66], given by,

$$J(x) = RMSE = \sqrt{\frac{1}{N}\sum_{i=1}^{N}\left(I_{exp}^{i} - I_{cal}^{i}(V_{exp}^{i}, x)\right)^2} \tag{7}$$

where N is the total number of measurements in the dataset. I_{exp} and V_{exp} denote the i-th empirical current and voltage values, respectively. x represents the decision variables (or solution vector) whose values have to be determined. $I_{cal}^{i}(V_{exp}^{i}, x)$ is the estimated value of the current output as a function of x; which characterizes the model described in Eq. (1).

To solve for the objective function in (7), the existing EA-based parameter extraction methods directly employ all five unknown parameters of the single diode model as decision parameters (i.e. $x = [I_{pv}, I_o, a, R_s, R_p]$). The approach leads to a search space with many dimensions. Depending on the complexity of the search surface, the vectors tend to become trapped in local optimal solutions [52,59]. Furthermore, due to the sheer number of candidate solutions that the optimizer has to examine, the parameter extraction process is time-consuming and prone to inconsistency issues. Most computation methods require several thousand iterations to achieve satisfactory solution [10,42,53,55–58].

4.1. The proposed method

In this work, a three-point-based parameter extraction method is proposed. In contrast to the conventional curve-fitting approach, the computations are executed in two phases. First, three *pivot points*, i.e. $P1 = (V_1, I_1)$, $P2 = (V_2, I_2)$, and $P3 = (V_3, I_3)$, are selected from the experimental dataset. By forcing the algorithm to pass through these points exactly, the explicit expressions of I_{PV}, I_o and R_p as functions of a and R_s can be derived. As a result, the five unknown parameters in the model is reduced to two. In the second phase of the algorithm, the EA is utilized to adjust the remaining sections of the curve to achieve best fit. This can be accomplished simply by fine-tuning the values of a and R_s. Hence, computations involved are greatly reduced. Plus, since the search is confined within the prospective regions of the search space, this approach is significantly more accurate and consistent compared to the conventional curve-fitting procedure. As guideline, the *pivot points* are chosen to be close to the geometrically critical regions of the *I-V* curve, as depicted in Fig. 8. They provide crucial information on the magnitude and shape of the curve [60,67,68].

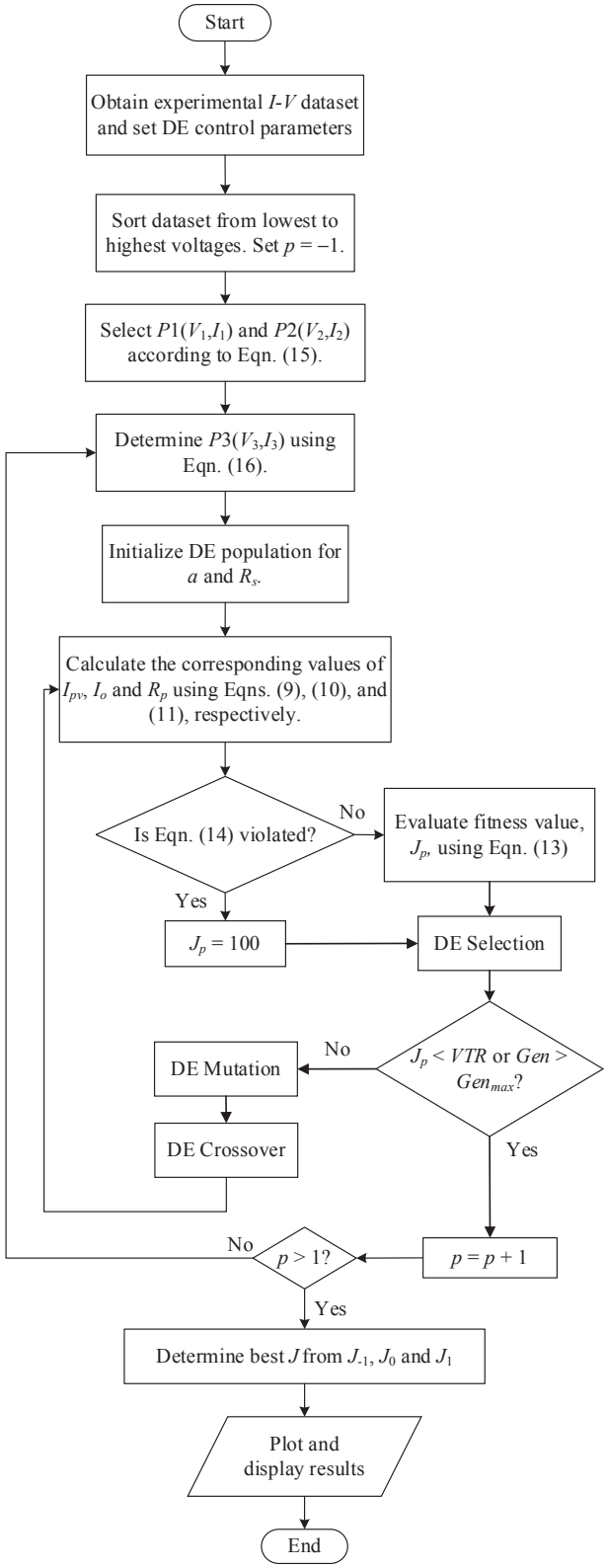

Fig. 9. Overall flowchart of proposed algorithm.

By substituting $P1$, $P2$ and $P3$ into Eq. (1), a system of equations can be formulated as follows:

$$I_i = I_{PV}N_p - I_oN_p\left(e^{\frac{V_i + I_iR_s(N_s/N_p)}{aV_t}} - 1\right) - \frac{V_i + I_iR_s(N_s/N_p)}{R_p(N_s/N_p)};\ i = 1,\ 2,\ 3 \tag{8}$$

Table 1
Parameter extraction results for 57-mm diameter R.T.C. France commercial silicon solar cell using the single diode model.

Parameters	Ref	I_{pv}	I_o (μ)	a	R_s	R_p	RMSE
Proposed method		0.76072	0.31911	1.47986	0.03629	54.19241	8.1291E−04
CSO	[32]	0.76078	0.323	1.48118	0.03638	53.7185	9.8602E−04
ISCE	[59]	0.760776	0.32302	1.48118	0.03638	53.7185	9.8602E−04
EHA-NMS	[69]	0.760776	0.32302	1.48118	0.03638	53.7185	9.8602E−04
STLBO	[32]	0.76078	0.32302	1.48114	0.03638	53.7187	9.8602E−04
Rcr-IJADE	[47]	0.760776	0.32302	1.48118	0.03638	53.7185	9.8602E−04
ABC-TRR	[77]	0.760776	0.32302	1.48118	0.03638	53.7185	9.8602E−04
ABC-DE	[72]	0.76077	0.32302	1.47986	0.03637	53.7185	9.8602E−04
NM-MPSO	[78]	0.76078	0.32306	1.4812	0.03638	53.7222	9.8602E−04
TLABC	[79]	0.76078	0.32302	1.48118	0.03638	53.7164	9.8602E−04
CWOA	[10]	0.76077	0.3239	1.4812	0.03636	53.7987	9.8602E−04
LMSA	[80]	0.7608	0.3185	1.4798	0.0364	53.3264	9.86E−04
PCE	[70]	0.760776	0.323021	1.481074	0.03638	53.7185	9.8602E−04
PSO	[78]	0.76077	0.32454	1.48165	0.03636	53.8550	9.8606E−04
BMO	[53]	0.76077	0.32479	1.48173	0.03636	53.8716	9.8608E−04
MABC	[55]	0.760779	0.321323	1.481385	0.03639	53.4000	9.8610E−04
ABC	[54]	0.7608	0.3251	1.4817	0.0364	53.6433	9.8620E−04
GOTLBO	[71]	0.76078	0.331552	1.48382	0.03627	54.1154	9.8744E−04
GGHS	[49]	0.76092	0.3262	1.48217	0.03631	53.0647	9.9097E−04
ABSO	[52]	0.7608	0.30623	1.47583	0.03659	52.2903	9.9124E−04
IGHS	[49]	0.76077	0.34351	1.4874	0.03613	53.2845	9.9306E−04
HS	[49]	0.7607	0.305	1.4754	0.0366	53.5946	9.95E−04
CPSO	[45]	0.7607	0.4	1.5033	0.0354	59.012	1.3900E−03
Newton	[34]	0.7608	0.3223	1.4837	0.0364	53.7634	9.70E−03
PS	[50]	0.7617	0.998	1.6	0.0313	64.1026	0.0149
SA	[39]	0.762	0.4798	1.5172	0.0345	43.1034	0.019
GA	[54]	0.7619	0.8087	1.5751	0.0299	42.3729	0.019
BFA	[54]	0.7602	0.8000	1.6951	0.0325	50.8691	0.029

Table 2
Point-by-point comparison between computed and experimental *I-V* data for 57-mm diameter R.T.C. France commercial silicon solar cell.

Data point	V_{exp}	I_{exp}	I_{cal}	Absolute error
1	−0.2057	0.764	0.7640	0.0000
2	−0.1291	0.762	0.7626	0.0006
3	−0.0588	0.7605	0.7613	0.0008
4	0.0057	0.7605	0.7601	0.0004
5	0.0646	0.76	0.7590	0.0010
6	0.1185	0.759	0.7580	0.0010
7	0.1678	0.757	0.7571	0.0001
8	0.2132	0.757	0.7561	0.0009
9	0.2545	0.7555	0.7551	0.0004
10	0.2924	0.754	0.7537	0.0003
11	0.3269	0.7505	0.7514	0.0009
12	0.3585	0.7465	0.7474	0.0009
13	0.3873	0.7385	0.7402	0.0017
14	0.4137	0.728	0.7275	0.0005
15	0.4373	0.7065	0.7071	0.0006
16	0.459	0.6755	0.6755	0.0000
17	0.4784	0.632	0.6311	0.0009
18	0.496	0.573	0.5724	0.0006
19	0.5119	0.499	0.4997	0.0007
20	0.5265	0.413	0.4137	0.0007
21	0.5398	0.3165	0.3173	0.0008
22	0.5521	0.212	0.2121	0.0001
23	0.5633	0.1035	0.1025	0.0010
24	0.5736	−0.0100	−0.0097	0.0003
25	0.5833	−0.1230	−0.1250	0.0020
26	0.59	−0.2100	−0.2100	0.0000
Sum of AE				0.0172
MAE				6.6155E−04
RMSE				8.1291E−04

Through algebraic substitution and manipulation, the explicit expressions for I_{pv}, R_p and I_o can be written as:

$$I_{PV} = \left[I_o N_p \left(e^{\frac{V_1 + I_1 R_s (N_s/N_p)}{aV_t}} - 1 \right) + \frac{V_1 + I_1 R_s (N_s/N_p)}{R_p (N_s/N_p)} + I_1 \right] \frac{1}{N_p} \tag{9}$$

$$R_p = \frac{(V_1 - V_2)(N_p/N_s) + R_s(I_1 - I_2)}{I_2 - I_1 - I_o N_p \left(e^{\frac{V_1 + I_1 R_s (N_s/N_p)}{aV_t}} - e^{\frac{V_2 + I_2 R_s (N_s/N_p)}{aV_t}} \right)} \tag{10}$$

$$I_o = \frac{\alpha(I_2 - I_1) + \beta(I_3 - I_1)}{N_p \left[\alpha \left(e^{\frac{V_1 + I_1 R_s (N_s/N_p)}{aV_t}} - e^{\frac{V_2 + I_2 R_s (N_s/N_p)}{aV_t}} \right) + \beta \left(e^{\frac{V_1 + I_1 R_s (N_s/N_p)}{aV_t}} - e^{\frac{V_3 + I_3 R_s (N_s/N_p)}{aV_t}} \right) \right]} \tag{11}$$

where

$$\alpha = V_3 - V_1 + R_s(N_s/N_p)(I_3 - I_1) \text{ and } \beta = V_2 - V_1 + R_s(N_s/N_p)(I_2 - I_1) \tag{12}$$

By back-substitution, Eqs. (9)–(11) provides the direct computation of I_o, R_p and I_{PV}, respectively. Thus, the complexity of the model is effectively reduced from five parameters to two, with the remaining unknowns being a and R_s. From the geometrical viewpoint, Eqs. (9)–(11) warrant that the computed *I-V* curve must pass through *P*1, *P*2 and *P*3 exactly. Therefore, the portions of the curve that have to be adjusted for best fit are reduced substantially.

In the second phase of the algorithm, DE is employed to search for the optimal values of a and R_s. These parameters are ideal to be utilized as the decision parameters due to their small parametric ranges and pronounced effects on the overall shape of the curve. By substituting $x = [a, R_s]$ into Eq. (7), the objective function of can be written as follows:

$$J(a, R_s) = RMSE = \sqrt{\frac{1}{N} \sum_{c=1}^{N} (f(V_{exp}, I_{exp}, a, R_s))^2} \tag{13}$$

Nonetheless, Eqs. (9)–(11) suggest that the certain sets of a and R_s values may yield non-physical (negative) values of I_{PV}, I_o, and R_p. To ensure the algorithm only considers feasible values of the parameters, the following conditions are imposed:

$$J = 100 \text{ if } \begin{matrix} I_{PV} < 0; \text{ or} \\ R_p < 0; \text{ or} \\ I_o < 0 \end{matrix} \tag{14}$$

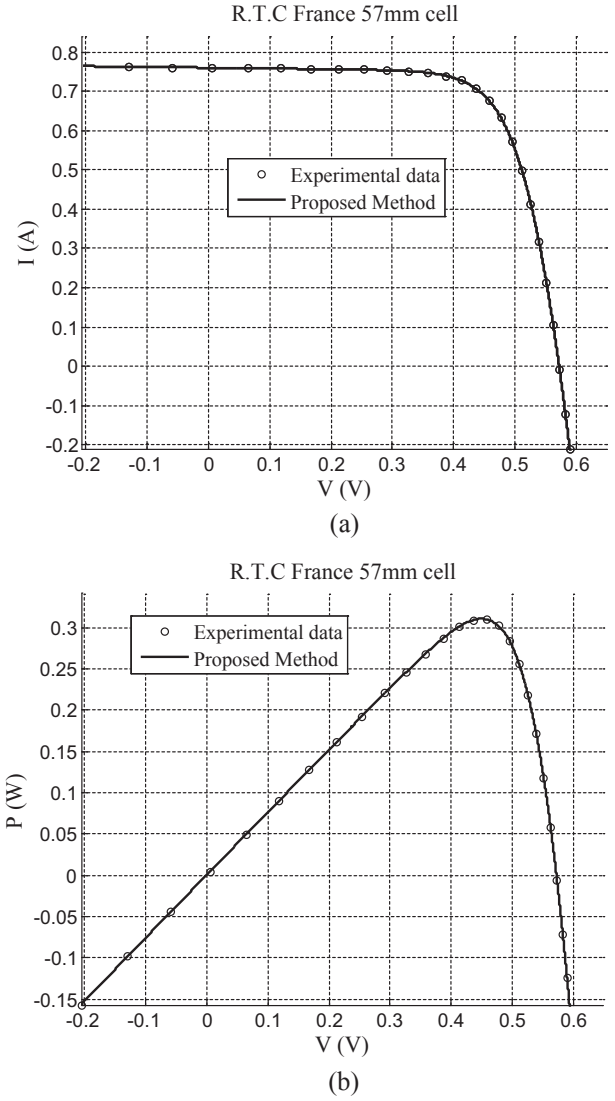

Fig. 10. Comparison between the experimental and computed (a) *I-V* and (b) *P-V* curves for 57-mm diameter R.T.C. France commercial silicon solar cell.

By this constraint, any vector that violates the limits specified in Eq. (14) is forced to assume an unusually large fitness value, i.e. 100. Since the algorithm is based on the minimization of the objective function, this prevents the violating vectors from being selected for the subsequent generation.

4.1.1. Selection of the Pivot Points

Depending on the measurement scheme, selecting the pivot points may be non-trivial. In this section, a simple procedure is introduced to choose $P1$, $P2$ and $P3$ from any set of measured *I-V* dataset.

First, the dataset is sorted in ascending voltage values. To gauge the gradient of the curve near the short- and open circuit regions, the first and last points of the dataset are assigned as $P1$ and $P2$, respectively, given by,

$$P1 = (V_1, I_1) = (V_{exp}^1, I_{exp}^1); \text{ and } P2 = (V_2, I_2) = (V_{exp}^N, I_{exp}^N); \quad (15)$$

Next, $P3$ is chosen in the vicinity of MPP to approximate the knee of the *I-V* curve. Since $P3$ plays an important role in determining the overall fit, it is considered at three different points for best fit, as follows:

$$P3 = (V_{exp}^{MPP\_ind+\Delta ind_{exp}p}, I_{exp}^{MPP\_ind+\Delta ind_{exp}p}) \quad (16)$$

where Δind denotes the index interval between the selections of $P3$; its value is determined by rounding up 10 percent of N to the nearest integer, i.e. $\Delta ind = \text{round}(0.1 \cdot N)$. On the other hand, the variable p is an integer index, which varies between -1, 0 and 1. By shifting p as the algorithm progresses, $P3$ assumes the values of three different data points near MPP. Lastly, *MPP_ind* is the MPP index of the experimental dataset. It is determined as the maximum product of the experimental current and voltage values. The command to calculate *MPP_ind* can be written in MATLAB script as:

$$[MPP\_val, MPP\_ind] = \max(\tilde{V}_{exp} .* \tilde{I}_{exp}) \quad (17)$$

where $\tilde{V}_{exp}$ and $\tilde{I}_{exp}$represent the voltage and current vectors of the experimental dataset, respectively.

Nonetheless, it is not mandatory to select $P1$, $P2$ and $P3$ utilizing the algorithm described here; these points may also be chosen manually by the user. The overall flow of the proposed algorithm is depicted in Fig. 9. It is worthwhile to note that the proposed method does not employ any simplifications or assumptions in the computation of the model parameters, which is crucial to retain the accuracy of the single diode model. Furthermore, the proposed method does not require any additional information, other than the measured data points and knowledge on the number of series/parallel connected cells.

Table 4
Point-by-point comparison between computed and experimental *I-V* data for Schutten Solar STM6-40/36 monocrystalline PV module.

Data point	V_{exp}	I_{exp}	I_{cal}	Absolute error
1	0.118	1.663	1.6630	0.0000
2	2.237	1.661	1.6595	0.0015
3	5.434	1.653	1.6541	0.0011
4	7.26	1.65	1.6509	0.0009
5	9.68	1.645	1.6458	0.0008
6	11.59	1.64	1.6395	0.0005
7	12.6	1.636	1.6339	0.0021
8	13.37	1.629	1.6273	0.0017
9	14.09	1.619	1.6181	0.0009
10	14.88	1.597	1.6027	0.0057
11	15.59	1.581	1.5811	0.0001
12	16.4	1.542	1.5420	0.0000
13	16.71	1.524	1.5211	0.0029
14	16.98	1.5	1.4992	0.0008
15	17.13	1.485	1.4854	0.0004
16	17.32	1.465	1.4660	0.0010
17	17.91	1.388	1.3886	0.0006
18	19.08	1.118	1.1180	0.0000
Sum of AE				0.0210
MAE				0.001169
RMSE				0.001774

Table 3
Parameter extraction results for Schutten Solar STM6-40/36 monocrystalline PV module using the single diode model.

Parameter	Proposed method	CWOA [10]	CIABC [58]	ABC [54]	BMO [53]	STBLO [32]	Ref. [62]
I_{PV}	1.6632	1.7	1.676	1.6644	1.6646	1.7	1.4142
I_o (μ)	2.7698	1.6338	1.6642	1.5	1.4311	1.4127	1.6635
a	1.5656	1.5	1.4976	1.4866	1.4994	1.5	1.4986
R_s (m)	0.4186	5	4.4	4.99	5	5	4.879
R_p	16.7328	15.4	15.617	15.206	14.9371	15.4	15.419
RMSE	0.001774	0.0018	0.001819	0.001838	0.0019	0.0019	0.002181

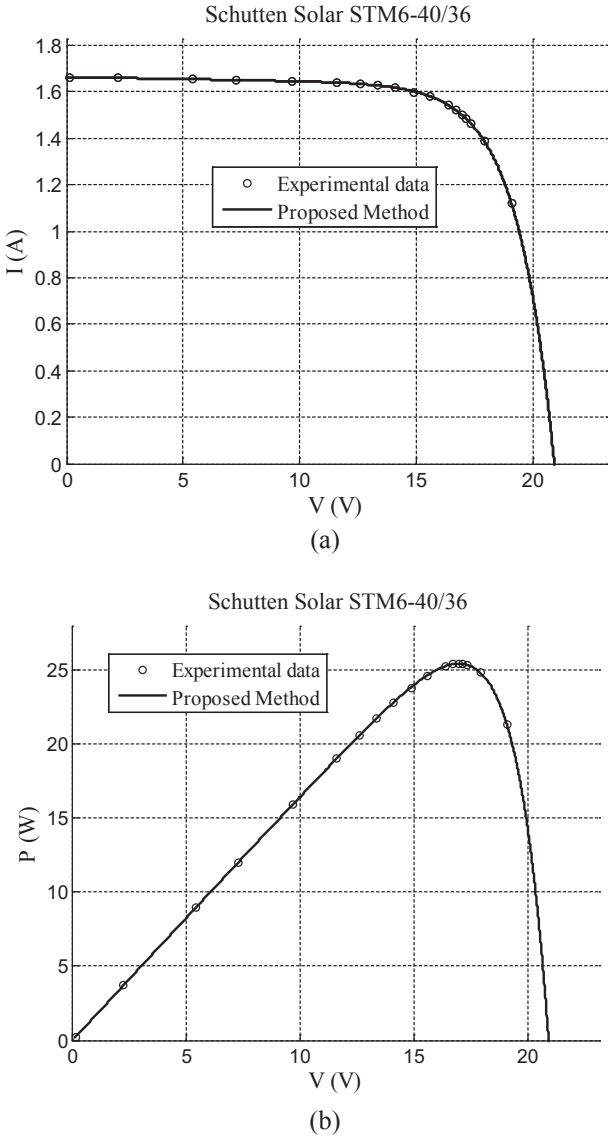

Fig. 11. Comparison between the experimental and computed (a) *I-V* and (b) *P-V* curves for Schutten Solar STM6-40/36 monocrystalline PV module.

5. Results and discussions

For successful implementation of DE, the control parameters have to be set appropriately. Based on extensive simulation trials, the optimal values of F and CR are set to be 0.7 and 0.8, respectively. There are no strict guidelines in selecting these values, but for most cases, $F > 0.4$ is recommended [65]. On the other hand, sufficiently large value of CR helps promote diversity in the population; which is especially useful there is a high correlation among the decision parameters [61]. Due to the efficient nature of the proposed method, NP and Gen_{max} can be set relatively low. In this work, both NP and Gen_{max} are set to 50. The DE strategy used is DE/best/1/bin. In this terminology, "best" indicates that the vector with the lowest fitness value is used as the base vector during the mutation process, "1" describes the number of difference vector, and "bin" denotes that the binomial crossover scheme is employed. The search ranges of the model parameters are set according to the related literature [10,11], i.e. $a \in [1, 2]$, $R_s \in [0, 0.5]$.

Table 6
Point-by-point comparison between computed and experimental *I-V* data for Schutten Solar STP6-120/36 polycrystalline PV module.

Data point	V_{exp}	I_{exp}	I_{cal}	Absolute error
1	9.06	7.45	7.4500	0.0000
2	9.74	7.42	7.4442	0.0242
3	10.32	7.44	7.4370	0.0030
4	11.17	7.41	7.4196	0.0096
5	11.81	7.38	7.3972	0.0172
6	12.36	7.37	7.3668	0.0032
7	12.74	7.34	7.3368	0.0032
8	13.16	7.29	7.2916	0.0016
9	13.59	7.23	7.2274	0.0026
10	14.17	7.1	7.1000	0.0000
11	14.58	6.97	6.9707	0.0007
12	14.93	6.83	6.8263	0.0037
13	15.39	6.58	6.5762	0.0038
14	15.71	6.36	6.3534	0.0066
15	16.08	6	6.0369	0.0369
16	16.34	5.75	5.7723	0.0223
17	16.76	5.27	5.2640	0.0060
18	16.9	5.07	5.0712	0.0012
19	17.1	4.79	4.7748	0.0152
20	17.25	4.56	4.5361	0.0239
21	17.41	4.29	4.2658	0.0242
22	17.65	3.83	3.8300	0.0000
Sum of AE				0.2091
MAE				0.009506
RMSE				0.014091

5.1. Modelling accuracy

5.1.1. Comparison with other related works

In this section, the algorithm is implemented in MATLAB for four case studies: (1) 57 mm silicon solar cell from R.T.C. France; (2) Schutten Solar STM6-40/36 monocrystalline module; and (3) Schutten STP6-120/36 polycrystalline module, (4) Photowatt-PWP 201 polycrystalline module. These datasets have been used extensively by other researchers as benchmarks to assess parameter extraction methods, for example [10,32,33,45,47,49,52,54,55,57–59,69–76]. The results from these works are included here for comparison.

A. Case 1: R.T.C. France 57-mm diameter commercial silicon cell

Case study 1 refers to the 57-mm diameter R.T.C. France commercial silicon solar cell. The dataset was measured under 1 sun (1000 W/m^2) at 33 °C [34] and comprises 26 pairs of *I-V* data points ($N = 26$). By utilizing the procedure discussed in Section 4.1.1, data points 1, 16 and 26 are chosen as $P1$, $P2$ and $P3$, respectively. Table 1 presents a comparison of the results computed using the proposed method and other

Table 5
Parameter extraction results for Schutten Solar STP6-120/36 polycrystalline PV module using the single diode model.

Parameter	Proposed method	STBLO [32]	CIABC [58]	BMO [53]	CWOA [10]	Ref. [62]	ABC [54]
I_{PV}	7.4830	7.4814	7.484126	7.4763	7.476	7.4838	7.476291
I_o (μ)	0.8868	1.1679	1.29	1.2333	1.2	1.2	1.2
a	1.1872	1.2048	1.214854	1.2092	1.2069	1.2072	1.206992
R_s (m)	5.3819	5.5	5.1	4.9	4.9	4.9	4.91
R_p	10.5309	9.8	9.89	9.7	9.7942	9.745	9.7
RMSE	0.014091	0.016211	0.016287	0.016985	0.017601	0.017879	0.019174

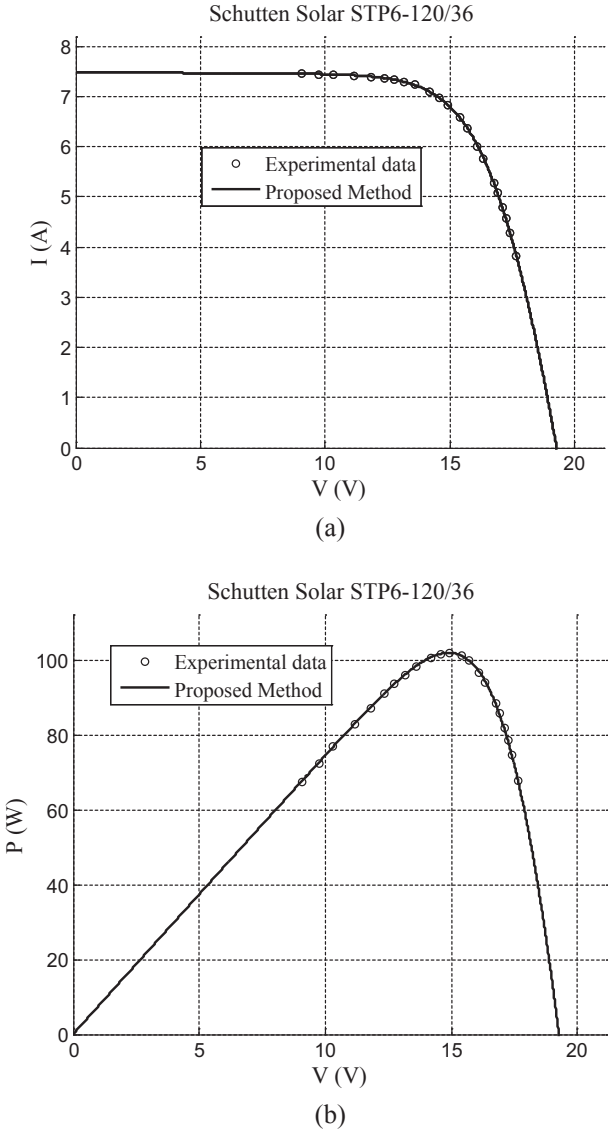

Fig. 12. Comparison between the experimental and computed (a) *I-V* and (b) *P-V* curves for Schutten Solar STP6-120/36 polycrystalline PV module.

relevant works for the R.T.C. France solar cell. It can be observed that, although the parameters values obtained by the proposed method are relatively close to those reported by other works, the former achieves the most accurate results, i.e. RMSE value of 8.1291E–04 A. In comparison, the RMSE of other state-of-the-art algorithms such as CSO [32], ISCE [59], EHA-NMS [69], STLBO [32], Rcr-IJADE [47], ABC-TRR [77], ABC-DE [72], NM-MPSO [78], TLABC [79], CWOA [10] are capped at 9.8602E–04 A. On the other hand, SA [39] and PS [50] obtained the least accurate results, with RMSE values of 0.019 A and 0.0149 A, respectively.

Table 8
Point-by-point comparison between computed and experimental *I-V* data for Photowatt-PWP 201 polycrystalline PV module.

Data point	V_{exp} (V)	I_{exp} (A)	I_{cal} (A)	Absolute error (A)
1	0.1248	1.0315	1.0315	0.0000
2	1.8093	1.03	1.0291	0.0009
3	3.3511	1.026	1.0268	0.0008
4	4.7622	1.022	1.0246	0.0026
5	6.0538	1.018	1.0224	0.0044
6	7.2364	1.0155	1.0197	0.0042
7	8.3189	1.014	1.0160	0.0020
8	9.3097	1.01	1.0103	0.0003
9	10.2163	1.0035	1.0009	0.0026
10	11.0449	0.988	0.9856	0.0024
11	11.8018	0.963	0.9614	0.0016
12	12.4929	0.9255	0.9255	0.0000
13	13.1231	0.8725	0.8755	0.0030
14	13.6983	0.8075	0.8102	0.0027
15	14.2221	0.7265	0.7303	0.0038
16	14.6995	0.6345	0.6381	0.0036
17	15.1346	0.5345	0.5364	0.0019
18	15.5311	0.4275	0.4286	0.0011
19	15.8929	0.3185	0.3177	0.0008
20	16.2229	0.2085	0.2064	0.0021
21	16.5241	0.101	0.0966	0.0044
22	16.7987	−0.008	−0.0100	0.0020
23	17.0499	−0.111	−0.1127	0.0017
24	17.2793	−0.209	−0.2105	0.0015
25	17.4885	−0.303	−0.3030	0.0000
Sum of AE				0.0505
MAE				0.002020
RMSE				2.422747E−03

Table 2 shows a point-by-point comparison between the experimental dataset and the computed *I-V* curve using the proposed method. The mean absolute error (MAE) between the two datasets is only 6.6155E–4 A. It is interesting to note that the AEs at *P*1, *P*2, and *P*3 (i.e. the data points 1, 16 and 26) are equal to zero. This indicates that the computed *I-V* curve passes through the three points exactly, which is in accordance to the premise described in Section 4.1. For graphical verification, the computed and experimental data are plotted in the same graph, as shown in Fig. 10. The figures show that both *I-V* and *P-V* curves computed by the proposed method are in very close agreement with the experimental data.

B. Case 2: Schutten Solar STM6-40/36 Monocrystalline

For case 2, the Schutten Solar STM6-40/36 commercial PV module, which comprises 36 monocrystalline cells (of size 38 mm × 128 mm) in series, is considered. The experimental dataset consists of 18 points and was measured at $T = 51$ °C [62]. For this dataset, data points 1, 12 and

Table 7
Parameter extraction results for Photowatt-PWP 201 polycrystalline PV module using the single diode model.

Parameters	I_{pv}	I_o (μ)	a	R_s	R_p	RMSE
Proposed method	1.03353	2.12479	1.30017	0.03471	19.37196	2.422747E−03
ISCE [59]	1.03051	3.48226	1.35119	0.03337	27.27729	2.425075E−03
EHA-NMS [69]	1.03051	3.48226	1.35119	0.03337	27.27728	2.425075E−03
Rcr-IJADE [47]	1.03051	3.48226	1.35119	0.03337	27.27728	2.425075E−03
ABC-TRR [77]	1.03051	3.48226	1.35119	0.03337	27.27728	2.425E−03
TLABC [79]	1.03056	3.4715	1.35087	0.03338	27.02599	2.42507E−03
MPCOA [81]	1.03188	3.37370	1.34740	0.03342	23.60258	2.4251E−03
FPA [82]	1.03209	3.04754	1.33698	0.03382	22.53811	2.7425E−03
ABC-DE [72]	1.0318	3.2774	1.3443	0.03351	23.47915	3.8855E−03
Newton [34]	1.0318	3.2876	1.34583	0.03349	15.26250	5.6010E−01

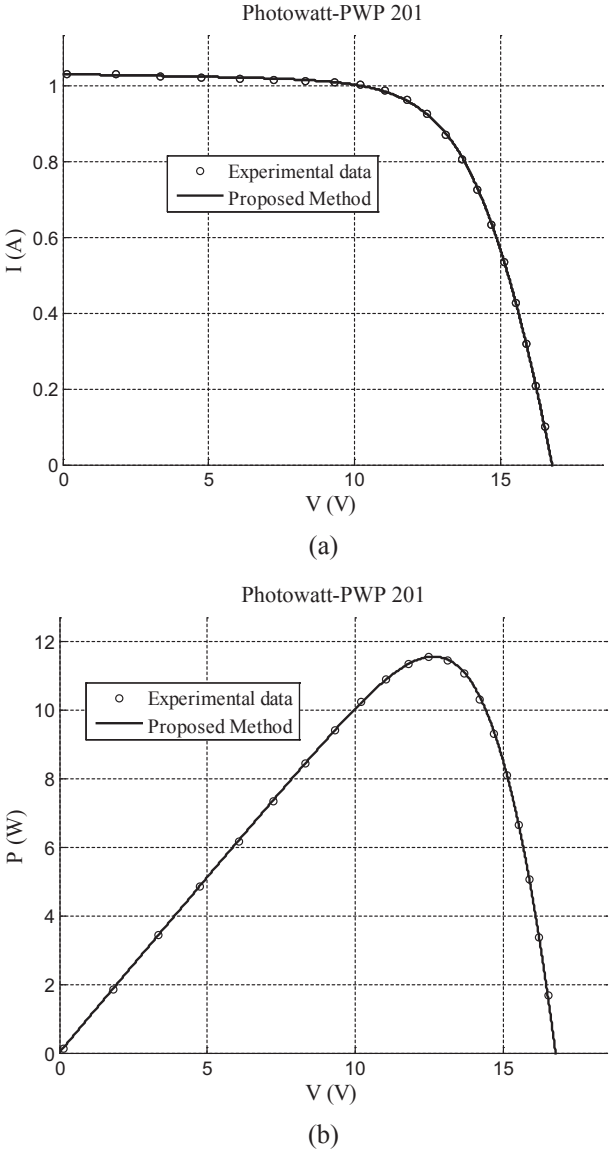

Fig. 13. Comparison between the experimental and computed (a) *I-V* and (b) *P-V* curves for Photowatt-PWP 201 polycrystalline PV module.

18 are chosen as *P*1, *P*2 and *P*3, respectively. Table 3 presents a comparison between the results obtained using the proposed method and values reported elsewhere. Additionally, the point-by-point comparison between the computed *I-V* curve and the experimental data are given in Table 4. Despite the irregular distribution of the measurement points, the proposed method manages to extract highly accurate parameters values. Specifically, the RMSE of the proposed is only 0.001774 A, which is lower that the values reported in CWOA [10], CIABC [58], ABC [54], BMO [53], STBLO [32], Ref. [62]. Moreover, the MAE of the computed *I-V* curve is only 0.001169 A. Fig. 11 shows that the *I-V* and *P-V* curves computed by the proposed method closely coincide with the experimental data.

C. Case 3: Schutten Solar STP6-126/36 Polycrystalline

In another case, the proposed method is utilized to extract the parameters of the Schutten Solar STP6-120/36 commercial PV module, which contains 36 polycrystalline cells (of size 156 mm × 156 mm) connected in series. The dataset contains 22 data points measured at $T = 55\,^{\circ}\mathrm{C}$ [62]. For this dataset, data points 1, 10 and 22 are selected as *P*1, *P*2 and *P*3, respectively. Table 5 presents a comparison of the

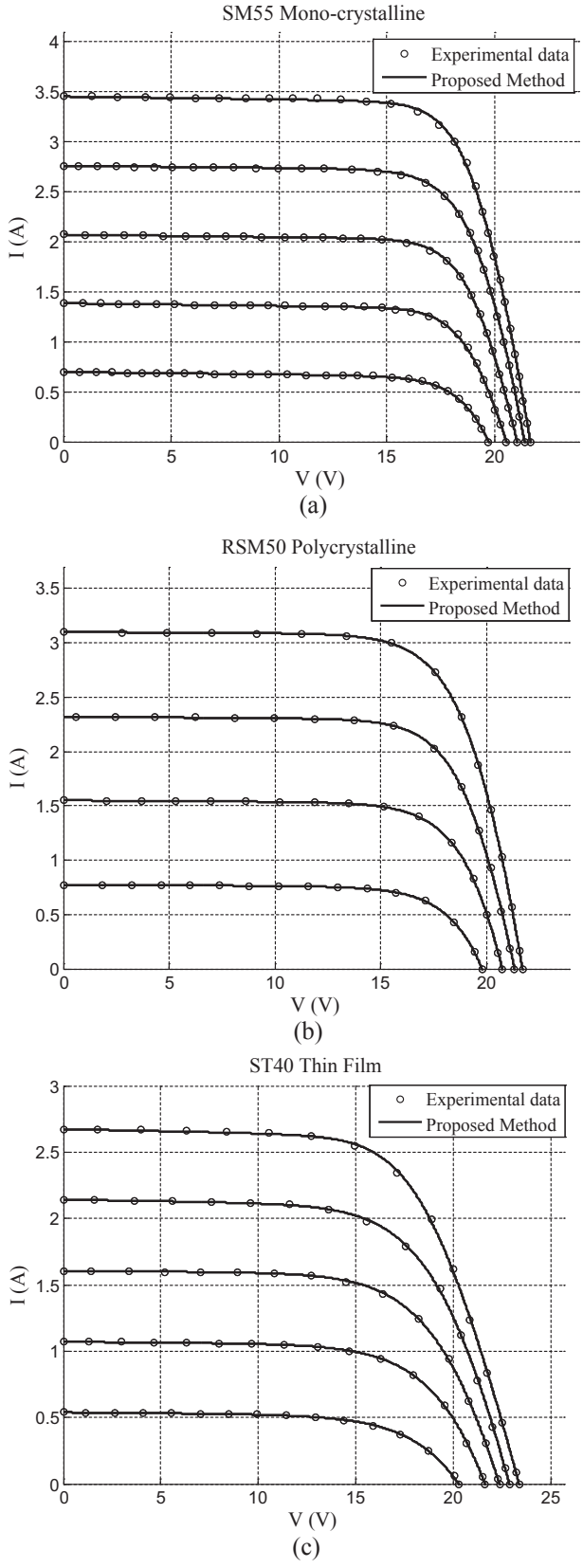

Fig. 14. Comparison between the experimental and computed *I-V* curves at varying irradiance for: (a) SM55 (b) RSM50 (c) ST40.

parameters and RMSE values obtained by various methods. With RMSE of 0.014091 A, the proposed method substantially outperforms STBLO [32], CIABC [58], BMO [53], CWOA [10], Ref. [62], and ABC [54].

Table 9
The extracted parameters for three types of PV modules at varying irradiance using the proposed method.

Parameter	Monocrystalline SM55	Polycrystalline RSM50*	Thin film ST40
G = 1000 W/m²			
I_{PV}	3.4599	3.1013	2.6840
I_o	4.0860E−10	6.4491E−07	1.3291E−07
a	1.0255	1.5256	1.2888
R_s	0.0138	0.0110	0.0306
R_p	9.2737	25.9257	7.5466
RMSE	0.0147	0.0051	0.0132
G = 800 W/m² (750 W/m²)			
I_{PV}	2.7655	2.3223	2.1459
I_o	1.0866E−08	9.8146E−08	9.6166E−06
a	1.1961	1.3589	1.7232
R_s	0.0125	0.0145	0.0223
R_p	11.7863	19.5725	10.2973
RMSE	0.0100	0.0080	0.0094
G = 600 W/m² (500 W/m²)			
I_{PV}	2.0761	1.5506	1.6062
I_o	3.3490E−10	7.7853E−07	1.8133E−05
a	1.0104	1.5479	1.8206
R_s	0.0176	0.0085	0.0219
R_p	10.7546	23.2062	24.8726
RMSE	0.0067	0.0018	0.0071
G = 400 W/m² (250 W/m²)			
I_{PV}	1.3870	0.7729	1.0716
I_o	2.9842E−10	1.2012E−06	2.6557E−05
a	1.0000	1.6028	1.8933
R_s	0.0214	0.0046	0.0168
R_p	10.9664	26.9681	19.5282
RMSE	0.0091	0.0020	0.0041
G = 200 W/m²			
I_{PV}	0.6969	–	0.5391
I_o	1.6012E−08	–	4.2910E−05
a	1.2175	–	2.0000
R_s	0.0122	–	0.0119
R_p	11.3203	–	18.1016
RMSE	0.0029	–	0.0037

Meanwhile, a point-by-point assessment of the curve is given in Table 6. The results show that the error is kept very low throughout the length of the curve. In particular, the MAE is found to be only 0.009506 A. Fig. 12 shows an overlay of the experimental data points on the computed curves. The figure reveals that the computed output fits the data points very closely, even though the latter is only provided in the neighborhood of MPP.

D. Case 4: Photowatt-PWP 201 Polycrystalline

Case study 4 investigates the parameter extraction of the Photowatt-PWP 201 PV module, which consists of 36 polycrystalline cells connected in series. The dataset contains 25 pairs of *I-V* points, measured at $G = 1000\ \mathrm{W/m^2}$ and $T = 45\ ^\circ\mathrm{C}$. For this dataset, the 1st, 12th and 25th points are selected as *P*1, *P*2 and *P*3, respectively. Table 7 tabulates the parameters obtained by the proposed method; they are benchmarked against other relevant works in the literature. As with previous results, the parameters values computed by the proposed method are comparable to the values reported elsewhere. By examining the RMSE values, it is evident that the solution produced by the proposed method is the most accurate, followed closely by ISCE [59], EHA-NMS [69], Rcr-IJADE [47], ABC-TRR [77], TLABC [79] and MPCOA [81]. In contrast, the analytical approach, namely the Newton method [34] shows RMSE values up to two orders of magnitude higher that its metaheuristic competitors.

For more insights, a point-by-point comparison between the computed and experimental *I-V* curve data is presented in Table 8. The results indicate that the absolute error is kept very low, i.e. less than

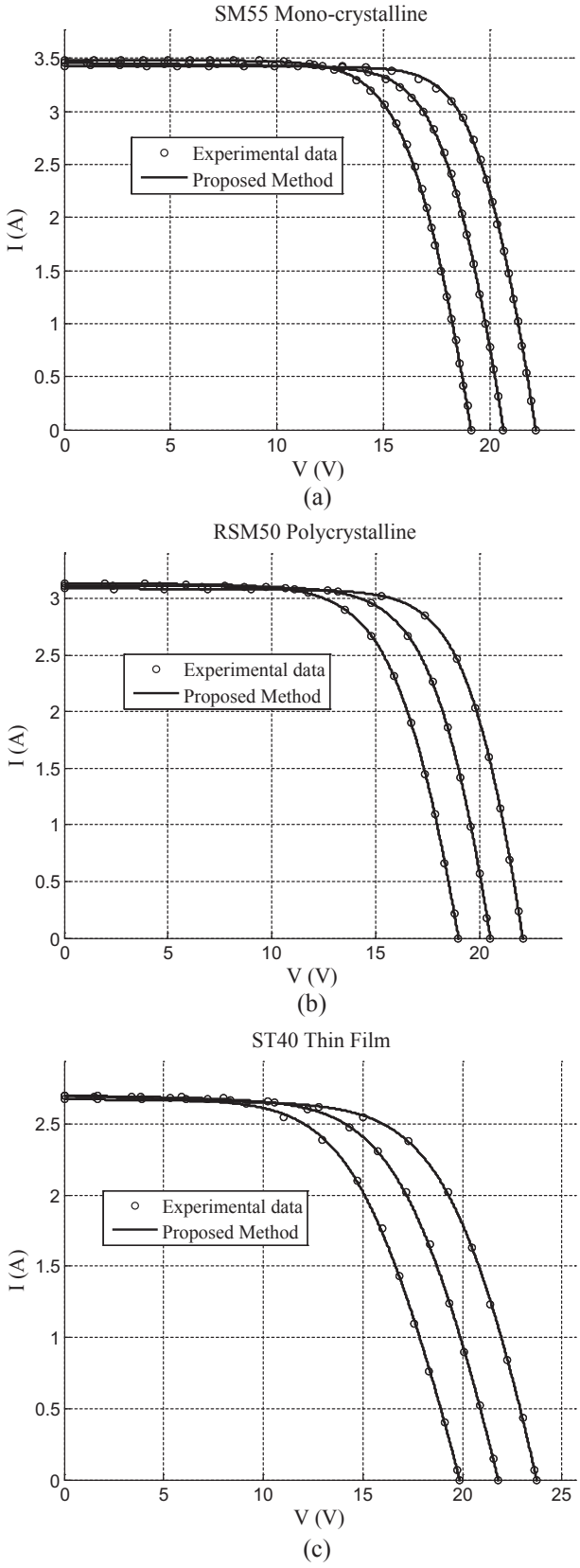

Fig. 15. Comparison between the experimental and computed *I-V* curves at varying temperature for: (a) SM55 (b) RSM50 (c) ST40.

0.005 A, across the entire voltage range. In addition, Fig. 13 shows the computed *I-V* and *P-V* curves against the experimental data for visual validation. As expected, the computed output matches well with the

Table 10
The extracted parameters for three types of PV modules at varying temperature using the proposed method.

Parameter	Monocrystalline SM55	Polycrystalline RSM50	Thin film ST40
$T = 20\,^{\circ}C$			
I_{PV}	3.4313	3.0904	2.6803
I_o	4.0257E−09	3.6626E−07	1.1220E−05
a	1.1842	1.5217	1.8078
R_s	0.0126	0.0105	0.0205
R_p	38.8324	27.8377	14.0211
RMSE	0.0110	0.0046	0.0094
$T = 40\,^{\circ}C$			
I_{PV}	3.4609	3.1132	2.7102
I_o	5.1806E−08	4.4288E−06	1.6194E−05
a	1.1793	1.5681	1.6015
R_s	0.0124	0.0098	0.0248
R_p	10.4048	40.5444	8.9450
RMSE	0.0122	0.0039	0.0099
$T = 60\,^{\circ}C$			
I_{PV}	3.4876	3.1377	2.7114
I_o	1.4339E−06	2.0489E−05	1.7976E−05
a	1.2569	1.5383	1.3847
R_s	0.0118	0.0114	0.0289
R_p	30.5499	17.9186	6.3831
RMSE	0.0130	0.0064	0.0148

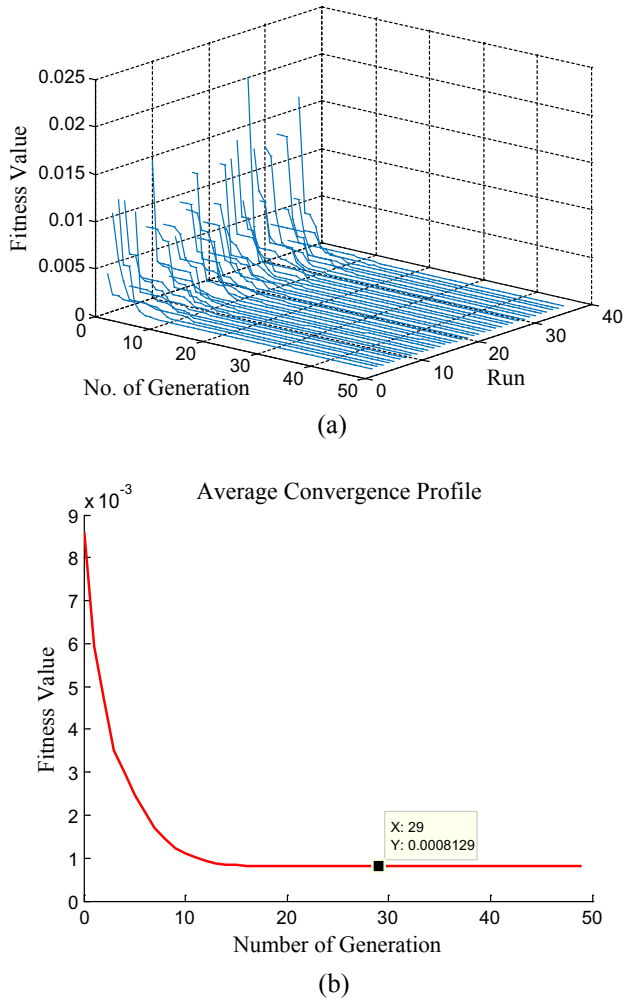

Fig. 16. Convergence characteristics of the proposed algorithm: (a) for each individual run, (b) the average profile over 35 runs.

experimental data points. In particular, the MAE of the *I-V* curve is only 0.002020 A.

5.1.2. Parameters extraction at different environmental conditions

To further demonstrate its practicality, the proposed method is used to extract the parameters of three commercial PV modules of different technologies, i.e. Shell SM55 (monocrystalline), Shell RSM50 (polycrystalline), and Shell ST40 (thin film). The experimental *I-V* datapoints of these modules are extracted from their respective manufacturer datasheets [83]. Fig. 14 presents the computed and experimental *I-V* curves of the modules at multiple levels of G, with T fixed at 25 °C. The corresponding values of the parameters are tabulated in Table 9. Note that, in the table, the corresponding values of G for RSM50 are shown in brackets (as indicated by the asterisk). On the other hand, the performance of the proposed method at varying T are given in Fig. 15. In this case, G is kept constant at 1000 W/m^2. The parameters values obtained at different T are shown in Table 10.

As evident in the figures, the computed curves maintain strong agreement with the experimental data points, even as the operating conditions deviate from the STC. The information on the performance of the PV modules at low irradiances and high temperature is especially crucial because the irradiance level throughout the day is often much lower than 1000 W/m^2 [84–86], while the temperature on the module surface easily rises above 50 °C during the midday [87]. Moreover, the model accuracy at lower irradiances is vital for partial shading studies [88]. Overall, the proposed method exhibits excellent accuracy—the RMSE is less than 0.02 A in all cases. Additionally, the series resistance of the thin film module (ST40) is observed to be generally higher than that of the crystalline modules; this is consistent with the findings reported in other studies [17,27]. Besides, PV modules have characteristically low series resistance and high shunt resistance, which is well reflected in the extracted results.

5.2. Computation speed

Similar to other members of the EA family, DE involves stochastic elements in its computation. Thus, it does not yield the same exact solution on every run. To assess the consistency of its computation, the proposed algorithm is executed 35 times and the results are examined. The dataset from Case 1 is used as an example.

Fig. 16 presents the convergence characteristics for each individual run and the average profile over 35 runs, respectively. As indicated in Fig. 16(a), the algorithm often initializes with very low fitness values (lowest recorded being $J = 0.018$). There are few cases where the initial value of J is relatively high (such as run 9, 26 and 35), but the algorithm manages to improve the solution and converge within low number of iterations. Fig. 16(b) shows that the algorithm always converges to $J = 8.129 \times 10^{-4}$ within 30 generations, irrespective of the initial conditions. This is a remarkable improvement in comparison to the existing curve-fitting algorithms, which often require few thousands of iterations and long computation times to approach convergence [10,53,55,58]. The average elapsed time for each run using the proposed method is only 1.023 s on a computer with Intel Core i7-4790 3.60 GHz processor, 16 GB RAM and Windows 10 Home 64-bit operating system.

5.3. Algorithm consistency

Fig. 17 presents the decision variables and fitness values computed by the algorithm over 35 independent runs. Since the values of the rest of the model parameters are directly calculated based on a and R_s, their values are not included here for brevity. From the figures, it can be noted that the parameters consistently converge in a very concentrated region of the search space. This suggests that the proposed algorithm is highly successful in locating the global optimal/suboptimal solution on

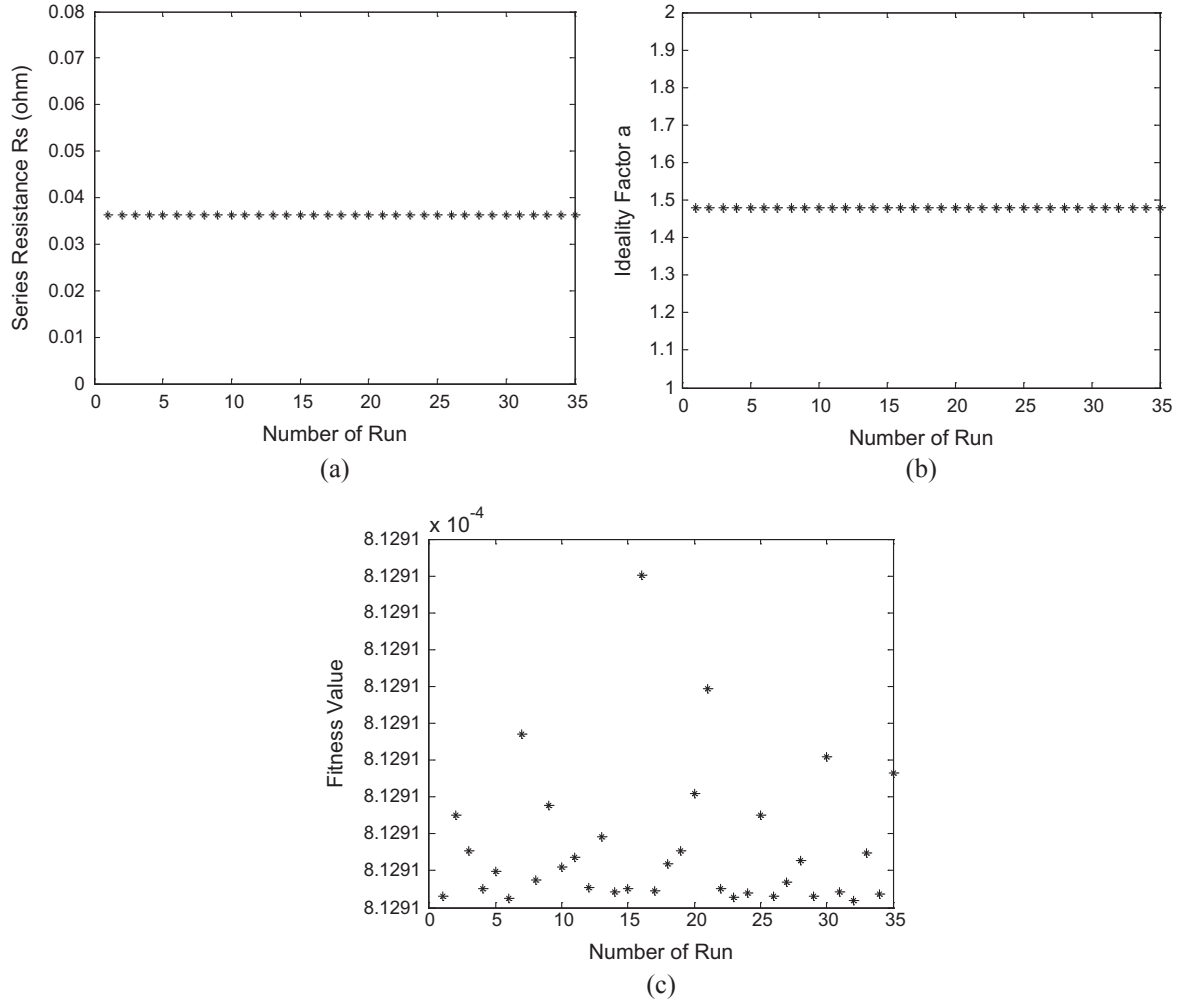

Fig. 17. The decision variables and fitness values obtained over 35 independent runs for R.T.C France 57 mm diameter solar cell: (a) series resistance (b) ideality factor (c) fitness value.

Table 11
Mean and STD of the parameters.

Cases		a	R_s	Fitness (J)
R.T.C France 57mm diameter solar cell	Mean	1.4799	0.0363	8.1291E−04
	STD	1.3117E−06	5.7945E−08	1.9106E−12
Schutten Solar STM6-40/36	Mean	1.5656	4.1856E−04	1.7736E−03
	STD	8.8709E−07	3.0559E−06	9.6277E−14
Schutten Solar STP6-120/36	Mean	1.1872	5.3818E−03	1.4091E−02
	STD	2.2699E−05	5.5602E−06	6.7960E−10
Photowatt-PWP 201	Mean	1.3002	0.03471	2.4227E−03
	STD	5.2869E−07	5.7619E−07	1.6581E−13

Table 12
Comparison in terms of STD of RMSE for R.T.C France 57mm diameter solar cell [10,54].

Algorithm	STD of RMSE
Proposed method	1.9106E−12
CWOA	1.0216E−08
STBLO	1.1333E−07
ABC	1.497E−05
BMO	3.986E−05
HS	0.7268
PSO	0.0289
GA	0.0735
BFA	0.0586

every run. For better insights, the mean and standard deviation (STD) of the parameters for all four cases considered in Section 5.1.1. are tabulated in Table 11. The STD can be interpreted as a stability index which reflects an algorithm's ability to reproduce the same results when executed multiple times. From the table, the values of the STDs are observed to be exceptionally low, i.e. less than 1×10^{-5} in all cases. These results indicate that the algorithm is very consistent; thus, a high-quality solution is always guaranteed.

Table 12 compares the STD of RMSE obtained by the proposed method and other EA-based parameter extraction methods for R.T.C France 57mm diameter solar cell [10,54]. As with the proposed method, the latter are executed for 35 times. However, instead of 50 iterations, the other algorithms are allowed to run for 10,000 iterations in order to obtain best possible solutions. Despite that, the proposed method achieves vastly superior consistency. Specifically, the STD in terms of RMSE is at least 4 order of magnitude lower than the competitors.

The exceptional performance of the algorithm can be attributed to several factors. First, by ensuring the model passes through three geometrically critical points of the dataset (i.e. via $P1$, $P2$ and $P3$), the vectors are initialized in the prospective regions of the search space; which explains the remarkably low initial values of J. Second, the implementation of the penalty function in DE (Eq. (5)) and parametric constraints (Eq. (14)) work in tandem to eliminate out-of-bound vectors during the optimization process. Thus, each iteration is executed

efficiently to explore the search space and physically meaningful solutions are guaranteed. Third, in order to prevent the vectors from getting trapped in local optima solutions, high values of *F* and *CR* are used promote diversity and exploration in the population [65]. Lastly, the one-to-one selection scheme utilized in DE eliminates any vectors that loses a single competition. As a result, only the best solutions are permitted to participate in creating the subsequent generation. Together, these factors contribute to highly accurate and consistent solutions.

6. Conclusion

In this paper, a new three-point-based approach to extract the parameters of the single diode model is presented. The main idea is to first warrant the model passes through three geometrically critical points on the *I-V* curve points exactly (and thus assumes the basic shape of the dataset). During the second phase of the computation, the optimizer is only utilized to adjust the intermediate sections of the *I-V* curve to achieve best fit. Hence, the computations involved are markedly simplified. In this work, DE is used as the optimizer for its outstanding global search capability, rapid convergence and few control parameters. For physically meaningful solutions, several parametric constraints are introduced to eliminate stray vectors during the optimization process.

The performance of the proposed method is extensively examined using four widely utilized experimental datasets. When compared to other relevant parameter extraction methods, the proposed method exhibits substantial improvement in terms of fitting accuracy. Considering that the exact parameters values for these datasets are not known, any reduction in the fitting error is highly valuable from the perspective of PV cell modelling. Further, tests on three other PV modules of different technologies (i.e. monocrystalline, polycrystalline, thin film) at varying environmental conditions indicate that the proposed method is reliable and suitable for practical applications. Besides, the proposed method is highly efficient—it consistently converges to the optimal solutions in less than 50 iterations, and the STD of the RMSE obtained over 35 runs is found to be at least 4 orders of magnitude lower than those reported in other works.

With these merits, the proposed method is envisaged to be valuable for practical applications where fast and reliable extraction of the PV cell/module parameters is required. For instance, the method can be applied for an online monitoring and fault detection of PV systems, in which the model parameters must be determined in real-time. Another potential application of the method is to shorten the computation time required for offline analysis (such as the study of solar cell degradation rate or cell fabrication process) where a large amount of measurement data is usually involved.

Acknowledgement

This work was funded by the Ministry of Higher Education, Malaysia, under the Rising Star Grant Award. The grant was managed by the Research Management Centre, Universiti Teknologi Malaysia, Skudai, Malaysia, under Vot. no. R.J130000.7823.4F919.

References

[1] Shafiee S, Topal E. When will fossil fuel reserves be diminished? Energy Policy 2009;37:181–9.
[2] Dti U. Meeting the energy challenge: A white paper on energy. Department for Trade and Industry, Cm7124; 2007.
[3] Tyagi VV, Rahim NAA, Rahim NA, Selvaraj JAL. Progress in solar PV technology: Research and achievement. Renew Sustain Energy Rev 2013;20:443–61.
[4] Nemet GF, O'Shaughnessy E, Wiser R, Darghouth N, Barbose G, Gillingham K, et al. Characteristics of low-priced solar PV systems in the U.S. Appl Energy 2017;187:501–13.
[5] Pvps I. Snapshot of global photovoltaic markets 2015. Report IEA-PVPS TI-29; 2016.
[6] Cervantes J, Choobineh F. Optimal sizing of a nonutility-scale solar power system and its battery storage. Appl Energy 2018;216:105–15.
[7] Secretariat R. Renewables 2018 Global Status Report. Renewables Global Status Report (GSR); 2018.
[8] Liang Y, Sun W, Zhu Y-G, Christie P. Mechanisms of silicon-mediated alleviation of abiotic stresses in higher plants: a review. Environ Pollut 2007;147:422–8.
[9] (ISE) FIfSES. Photovoltaics report; 2018.
[10] Oliva D, Abd El Aziz M, Ella Hassanien A. Parameter estimation of photovoltaic cells using an improved chaotic whale optimization algorithm. Appl Energy 2017;200:141–54.
[11] Yu K, Chen X, Wang X, Wang Z. Parameters identification of photovoltaic models using self-adaptive teaching-learning-based optimization. Energy Convers Manage 2017;145:233–46.
[12] Chin VJ, Salam Z, Ishaque K. An accurate modelling of the two-diode model of PV module using a hybrid solution based on differential evolution. Energy Convers Manage 2016;124:42–50.
[13] Yu F, Huang G, Lin W, Xu C. Lumped-parameter equivalent circuit model for S-shaped current-voltage characteristics of organic solar cells. IEEE Trans Electron Dev 2018;1–8.
[14] De Castro F, Laudani A, Fulginei FR, Salvini A. An in-depth analysis of the modelling of organic solar cells using multiple-diode circuits. Sol Energy 2016;135:590–7.
[15] Jain A, Kapoor A. A new approach to study organic solar cell using Lambert W-function. Sol Energy Mater Sol Cells 2005;86:197–205.
[16] Ben Or A, Appelbaum J. Estimation of multi-junction solar cell parameters. Prog Photovolt Res Appl 2013;21:713–23.
[17] Chin VJ, Salam Z, Ishaque K. An accurate and fast computational algorithm for the two-diode model of PV module based on hybrid method. IEEE Trans Ind Electron 2017;64:6212–22.
[18] Ram JP, Manghani H, Pillai DS, Babu TS, Miyatake M, Rajasekar N. Analysis on solar PV emulators: A review. Renew Sustain Energy Rev 2018;81:149–60.
[19] Zagrouba M, Sellami A, Bouaïcha M, Ksouri M. Identification of PV solar cells and modules parameters using the genetic algorithms: application to maximum power extraction. Sol Energy 2010;84:860–6.
[20] Sellami A, Bouaïcha M. Application of the genetic algorithms for identifying the electrical parameters of PV solar generators. In: Kosyachenko Leonid A, editor. Solar Cells-Silicon Wafer-Based Technologies, ISBN. 2011:978-53.
[21] Kennerud KL. Analysis of performance degradation in CdS solar cells. Aerospace and Electronic Systems, IEEE Transactions on. 1969; AES-5: 912-7.
[22] Ikegami T, Maezono T, Nakanishi F, Yamagata Y, Ebihara K. Estimation of equivalent circuit parameters of PV module and its application to optimal operation of PV system. Sol Energy Mater Sol Cells 2001;67:389–95.
[23] Ortiz-Conde A, García Sánchez FJ, Muci J. New method to extract the model parameters of solar cells from the explicit analytic solutions of their illuminated I-V characteristics. Sol Energy Mater Sol Cells 2006;90:352–61.
[24] Jamil WJ, Rahman HA, Shaari S, Salam Z. Performance degradation of photovoltaic power system: Review on mitigation methods. Renew Sustain Energy Rev 2017;67:876–91.
[25] Femia N, Petrone G, Spagnuolo G, Vitelli M. Power electronics and control techniques for maximum energy harvesting in photovoltaic systems. CRC Press; 2012.
[26] Park N, Oh W, Kim D. Effect of temperature and humidity on the degradation rate of multicrystalline silicon photovoltaic module. Int J Photoenergy 2013;2013.
[27] Ishaque K, Salam Z, Mekhilef S, Shamsudin A. Parameter extraction of solar photovoltaic modules using penalty-based differential evolution. Appl Energy 2012;99:297–308.
[28] Chin VJ, Salam Z, Ishaque K. Cell modelling and model parameters estimation techniques for photovoltaic simulator application: A review. Appl Energy 2015;154:500–19.
[29] Ishaque K, Salam Z, Taheri H, Shamsudin A. A critical evaluation of EA computational methods for Photovoltaic cell parameter extraction based on two diode model. Sol Energy 2011;85:1768–79.
[30] Muhsen DH, Ghazali AB, Khatib T, Abed IA. Parameters extraction of double diode photovoltaic module's model based on hybrid evolutionary algorithm. Energy Convers Manage 2015;105:552–61.
[31] Sandrolini L, Artioli M, Reggiani U. Numerical method for the extraction of photovoltaic module double-diode model parameters through cluster analysis. Appl Energy 2010;87:442–51.
[32] Guo L, Meng Z, Sun Y, Wang L. Parameter identification and sensitivity analysis of solar cell models with cat swarm optimization algorithm. Energy Convers Manage 2016;108:520–8.
[33] Lin P, Cheng S, Yeh W, Chen Z, Wu L. Parameters extraction of solar cell models using a modified simplified swarm optimization algorithm. Sol Energy 2017;144:594–603.
[34] Easwarakhanthan T, Bottin J, Bouhouch I, Boutrit C. Nonlinear minimization algorithm for determining the solar cell parameters with microcomputers. Int J Solar Energy 1986;4:1–12.
[35] Chan DSH, Phang JCH. Analytical methods for the extraction of solar-cell single- and double-diode model parameters from I-V characteristics. Electron Dev, IEEE Trans 1987;34:286–93.
[36] Chegaar M, Ouennoughi Z, Hoffmann A. A new method for evaluating illuminated solar cell parameters. Solid-State Electron 2001;45:293–6.
[37] Gow JA, Manning CD. Development of a photovoltaic array model for use in power-electronics simulation studies. Electr Power Appl, IEE Proc 1999;146:193–200.
[38] Saha P, Kumar S, Nayak SK, Sahu HS. Parameter estimation of double diode photovoltaic module. In: Power, Dielectric and Energy Management at NERIST (ICPDEN), 2015 1st Conference on: IEEE; 2015. p. 1–4.
[39] El-Naggar KM, AlRashidi MR, AlHajri MF, Al-Othman AK. Simulated Annealing algorithm for photovoltaic parameters identification. Sol Energy 2012;86:266–74.

[40] Jervase JA, Bourdoucen H, Al-Lawati A. Solar cell parameter extraction using genetic algorithms. Meas Sci Technol 2001;12:1922.
[41] Moldovan N, Picos R, Garcia-Moreno E. Parameter extraction of a solar cell compact model usign genetic algorithms. In: Electron Devices, 2009 CDE 2009 Spanish Conference on; 2009. p. 379–82.
[42] Ye M, Wang X, Xu Y. Parameter extraction of solar cells using particle swarm optimization. J Appl Phys 2009;105:094502.
[43] Hengsi Q, Kimball JW. Parameter determination of Photovoltaic Cells from field testing data using particle swarm optimization. In: Power and Energy Conference at Illinois (PECI), 2011 IEEE; 2011. p. 1–4.
[44] Jing Jun S, Kay-Soon L. Photovoltaic model identification using particle swarm optimization with inverse barrier constraint. Power Electron, IEEE Trans 2012;27:3975–83.
[45] Wei H, Cong J, Lingyun X, Deyun S. Extracting solar cell model parameters based on chaos particle swarm algorithm. In: Electric Information and Control Engineering (ICEICE), 2011 International Conference on: IEEE; 2011. p. 398–2.
[46] da Costa WT, Fardin JF, Simonetti DSL, Neto LdVBM. Identification of photovoltaic model parameters by Differential Evolution. Industrial Technology (ICIT). In: 2010 IEEE International Conference on; 2010. p. 931–6.
[47] Gong W, Cai Zhihua. Parameter extraction of solar cell models using repaired adaptive differential evolution. Sol Energy 2013;94.
[48] Ma J, Ting TO, Man KL, Zhang N, Guan S-U, Wong PWH. Parameter estimation of photovoltaic models via cuckoo search. J Appl Math 2013;2013:8.
[49] Askarzadeh A, Rezazadeh A. Parameter identification for solar cell models using harmony search-based algorithms. Sol Energy 2012;86:3241–9.
[50] AlHajri MF, El-Naggar KM, AlRashidi MR, Al-Othman AK. Optimal extraction of solar cell parameters using pattern search. Renew Energy 2012;44:238–45.
[51] AlRashidi MR, AlHajri MF, El-Naggar KM, Al-Othman AK. A new estimation approach for determining the I-V characteristics of solar cells. Sol Energy 2011;85:1543–50.
[52] Askarzadeh A, Rezazadeh A. Artificial bee swarm optimization algorithm for parameters identification of solar cell models. Appl Energy 2013;102:943–9.
[53] Askarzadeh A, Rezazadeh A. Extraction of maximum power point in solar cells using bird mating optimizer-based parameters identification approach. Sol Energy 2013;90:123–33.
[54] Oliva D, Cuevas E, Pajares G. Parameter identification of solar cells using artificial bee colony optimization. Energy 2014;72:93–102.
[55] Jamadi M, Merrikh-Bayat F, Bigdeli M. Very accurate parameter estimation of single- and double-diode solar cell models using a modified artificial bee colony algorithm. Int J Energy Environ Eng 2016;7:13–25.
[56] Wang G, Zhao K, Shi J, Chen W, Zhang H, Yang X, et al. An iterative approach for modeling photovoltaic modules without implicit equations. Appl Energy 2017;202:189–98.
[57] Yu K, Liang JJ, Qu BY, Cheng Z, Wang H. Multiple learning backtracking search algorithm for estimating parameters of photovoltaic models. Appl Energy 2018;226:408–22.
[58] Oliva D, Ewees AA, Aziz MAE, Hassanien AE, Peréz-Cisneros M. A chaotic improved artificial bee colony for parameter estimation of photovoltaic cells. Energies 2017;10:865.
[59] Gao X, Cui Y, Hu J, Xu G, Wang Z, Qu J, et al. Parameter extraction of solar cell models using improved shuffled complex evolution algorithm. Energy Convers Manage 2018;157:460–79.
[60] Villalva MG, Gazoli JR, Filho ER. Comprehensive approach to modeling and simulation of photovoltaic arrays. Power Electron, IEEE Trans 2009;24:1198–208.
[61] Wei H, Cong J, Lingyun X, Deyun S. Extracting solar cell model parameters based on chaos particle swarm algorithm. In: Electric Information and Control Engineering (ICEICE), 2011 International Conference on: IEEE; 2011. p. 398–02.
[62] Tong NT, Pora W. A parameter extraction technique exploiting intrinsic properties of solar cells. Appl Energy 2016;176:104–15.
[63] Chin VJ, Salam Z, Ishaque K. An improved method to estimate the parameters of the single diode model of photovoltaic module using differential evolution. In: Electric Power and Energy Conversion Systems (EPECS), 2015 4th International Conference on; 2015. p. 1–6.
[64] Das S, Suganthan PN. Differential evolution: a survey of the state-of-the-art. Evolut Comput, IEEE Trans 2011;15:4–31.
[65] Price K, Storn RM, Lampinen JA. Differential evolution: a practical approach to global optimization. Springer; 2006.
[66] Jiang LL, Maskell DL, Patra JC. Parameter estimation of solar cells and modules using an improved adaptive differential evolution algorithm. Appl Energy 2013;112:185–93.
[67] Siaw F-L, Chong K-K. A systematic method of interconnection optimization for dense-array concentrator photovoltaic system. Sci World J 2013;2013:11.
[68] Chin VJ, Salam Z, Ishaque K. An accurate two diode model computation for CIS thin film PV module using the hybrid approach. In: Electric Power and Energy Conversion Systems (EPECS), 2015 4th International Conference on; 2015. p. 1–6.
[69] Chen Z, Wu L, Lin P, Wu Y, Cheng S. Parameters identification of photovoltaic models using hybrid adaptive Nelder-Mead simplex algorithm based on eagle strategy. Appl Energy 2016;182:47–57.
[70] Zhang Y, Lin P, Chen Z, Cheng S. A population classification evolution algorithm for the parameter extraction of solar cell models. Int J Photoenergy 2016;2016.
[71] Chen X, Yu K, Du W, Zhao W, Liu G. Parameters identification of solar cell models using generalized oppositional teaching learning based optimization. Energy 2016;99:170–80.
[72] Hachana O, Hemsas KE, Tina GM, Ventura C. Comparison of different metaheuristic algorithms for parameter identification of photovoltaic cell/module. J Renew Sustain Energy 2013;5.
[73] Xu S, Wang Y. Parameter estimation of photovoltaic modules using a hybrid flower pollination algorithm. Energy Convers Manage 2017;144:53–68.
[74] Kler D, Sharma P, Banerjee A, Rana KPS, Kumar V. PV cell and module efficient parameters estimation using Evaporation Rate based Water Cycle Algorithm. Swarm Evol Comput 2017;35:93–110.
[75] Han W, Wang H-H, Chen L. Parameters identification for photovoltaic module based on an improved artificial fish swarm algorithm. Sci World J 2014;2014:859239.
[76] Abd Elaziz M, Oliva D. Parameter estimation of solar cells diode models by an improved opposition-based whale optimization algorithm. Energy Convers Manage 2018;171:1843–59.
[77] Wu L, Chen Z, Long C, Cheng S, Lin P, Chen Y, et al. Parameter extraction of photovoltaic models from measured I-V characteristics curves using a hybrid trust-region reflective algorithm. Appl Energy 2018;232:36–53.
[78] Hamid NFA, Rahim NA, Selvaraj J. Solar cell parameters identification using hybrid Nelder-Mead and modified particle swarm optimization. J Renew Sustain Energy 2016;8:015502.
[79] Chen X, Xu B, Mei C, Ding Y, Li K. Teaching–learning–based artificial bee colony for solar photovoltaic parameter estimation. Appl Energy 2018;212:1578–88.
[80] Dkhichi F, Oukarfi B, Fakkar A, Belbounaguia N. Parameter identification of solar cell model using Levenberg–Marquardt algorithm combined with simulated annealing. Sol Energy 2014;110:781–8.
[81] Yuan X, Xiang Y, He Y. Parameter extraction of solar cell models using mutative-scale parallel chaos optimization algorithm. Sol Energy 2014;108:238–51.
[82] Alam DF, Yousri DA, Eteiba MB. Flower pollination algorithm based solar PV parameter estimation. Energy Convers Manage 2015;101:410–22.
[83] Shell Solar Module Datasheets. Available: https://drive.google.com/drive/folders/1mt4mnxfLYqpNmaIGujObzRCwkz9FXxeE?usp=sharing; 2018.
[84] Lorenz E, Hurka J, Heinemann D, Beyer HG. Irradiance forecasting for the power prediction of grid-connected photovoltaic systems. Selected Top Appl Earth Observ Remote Sens, IEEE J 2009;2:2–10.
[85] Mattei M, Notton G, Cristofari C, Muselli M, Poggi P. Calculation of the polycrystalline PV module temperature using a simple method of energy balance. Renew Energy 2006;31:553–67.
[86] Almaktar M, Abdul Rahman H, Hassan MY. Saeh I. Artificial neural network-based photovoltaic module temperature estimation for tropical climate of Malaysia and its impact on photovoltaic system energy yield. Progr Photovolt: Res Appl 2013. n/a-n/a.
[87] Kurtz S, Whitfield K, TamizhMani G, Koehl M, Miller D, Joyce J, et al. Evaluation of high-temperature exposure of photovoltaic modules. Prog Photovolt Res Appl 2011;19:954–65.
[88] Prasanth Ram J, Rajasekar N. A new robust, mutated and fast tracking LPSO method for solar PV maximum power point tracking under partial shaded conditions. Appl Energy 2017;201:45–59.

Shell Solar Energy B.V.
P.O. Box 849
5700 AV Helmond
The Netherlands
Tel. (31) 492 - 508 608
Fax. (31) 492 - 508 600
E-mail. solarinfo@si.shell.com

Product Information Sheet Solar Module RSM 50

General

The solar module contains 36 series connected 10x10 cm^2 multicrystalline silicon solar cells, generating a nominal peak power of 48 watt at 17 volt.
One single RSM 50 solar module can charge a 12 volt battery using a charge regulator. System voltages of 24 volt and higher can be obtained by connecting modules in series. Higher currents can be obtained by connecting modules in parallel.

Mechanical construction

The front of the solar module is a high impact resistant, highly transparent tempered glass plate offering the solar module excellent protection against environmental hazards such as hail, snow, ice and storms.
The back of the solar module consists of a Tedlar®-aluminium-polyester foil, offering a reliable barrier against penetration of moisture and dirt.
The solar cells are embedded in ultraviolet stabilised ethyl vinyl acetate (EVA). The highly corrosion-resistant aluminium alloy frame provides structural support for the solar module.

Junction box

The Makrolon junction box provides a high quality, dust and watertight IP65-rated housing for the rigid connection block and is fitted with two PG16 cable glands. These cable glands can be used for cables with an outside diameter from ø10 mm up to ø14 mm maximum.
Never use the junction box as a grip to carry the solar module!

Connection block

Inside the junction box there is a five pole connection block with two bypass diodes, offering a suitable “hot spot” protection of the solar cells.
The terminals are coded NC, (+), (¤) and (-).
The NC is a “not connected” terminal and can be used for interconnection purposes.
***Never connect any external wiring to the terminal coded* (¤).** This terminal is used for internal wiring only.

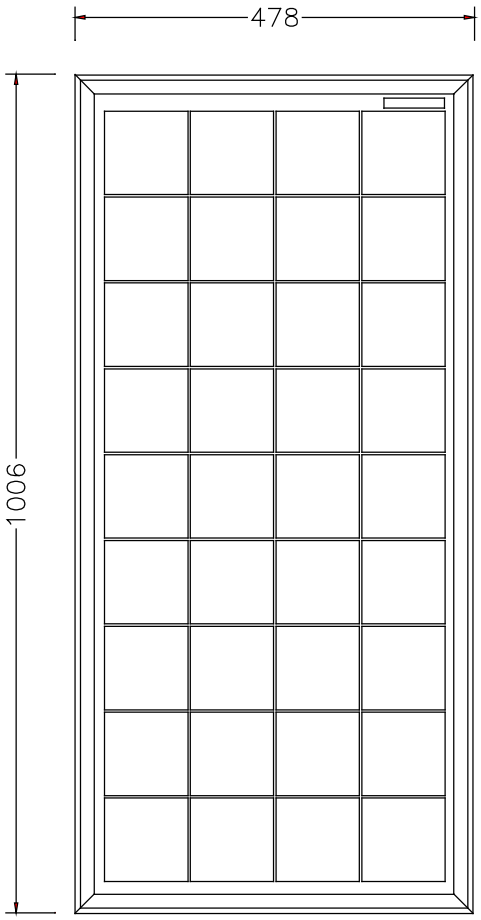

Qualifications and Certificates

The solar modules meet the requirements of the following qualification test standards:

- The Photovoltaic Modules Test Specification IEC 61215.
- The salt spray test according to IEC 68-2-11 (test Ka)

ISO 9001

JOINT RESEARCH CENTRE EUROPEAN COMMISSION

CE

DSO 004-01 / 20000316

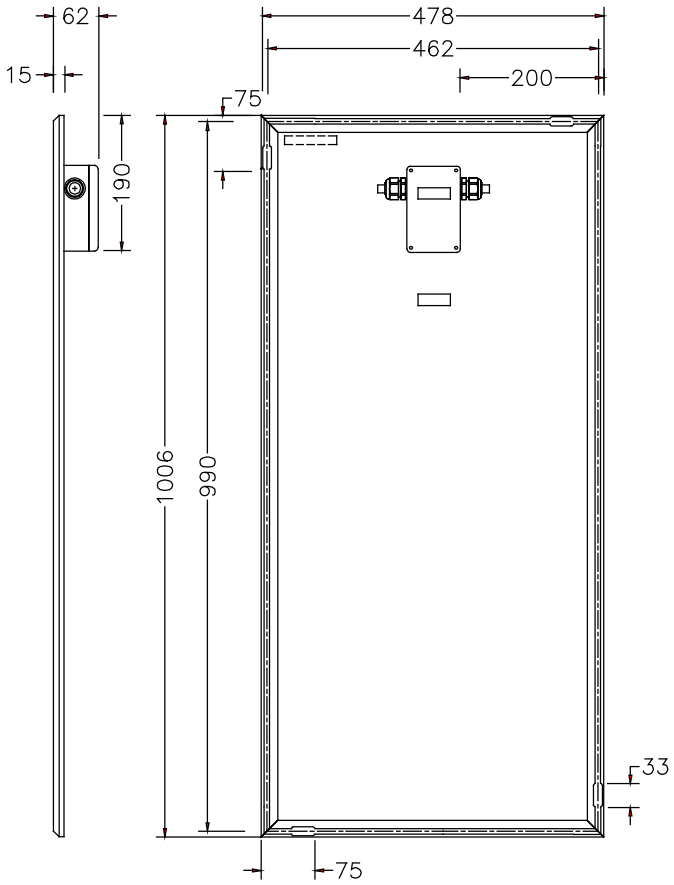

Mechanical specifications

The drawing above shows the side and back views of the RSM 50 solar module.
The aluminium frame is provided with a slot on each side of the frame in which tee bolts can be inserted. The tee bolts (with square heads) are able to slide over almost the entire length of the frame. This provides a simple and easy to use mounting method for fixing the solar module to mechanical constructions.

For mounting purposes a set of 4 tee bolts M6x25 mm, washers M6 and nuts M6 is supplied together with each solar module.

Outside dimensions	:	1006 x 478 mm
Thickness (Including junction box)	:	62 mm
Thickness (Aluminium frame)	:	15 mm
Weight	:	5.2 kg

Electrical characteristics

Typical data at Standard Test Conditions (STC):
(1000 W/m² irradiance level, AM 1.5 spectrum and 25 °C cell temperature)

Nominal peak power	(P_{mpp})	:	48	W
Peak power voltage	(V_{mpp})	:	17.0	V
Peak power current	(I_{mpp})	:	2.8	A
Short circuit current	(I_{sc})	:	3.1	A
Open circuit voltage	(V_{oc})	:	21.7	V

The tolerance on the peak power is ± 4 %

The calibration of the measurements at STC is traceable to the standard of the 'European Solar Test Installation' (ESTI) dated November 1, 1997.

The abbreviation 'mpp' stands for Maximum Power Point.

Typical data at Nominal Operating Cell Temperature (NOCT) conditions:
(800 W/m² irradiance level, AM 1.5 spectrum, wind velocity 1 m/s, T_{amb} 20 ºC)

T_{NOCT}	:	44	°C
P_{mpp}	:	35	W
V_{mpp}	:	15.4	V
I_{sc}	:	2.5	A
V_{oc}	:	19.7	V

Temperature coefficients:

α P_{mpp}	:	-0.4	%/°C
α V_{mpp}	:	-78	mV/°C
α I_{sc}	:	+1	mA/°C
α V_{oc}	:	-78	mV/°C

The relative reduction of module efficiency is 12% at an irradiance of 200 W/m^2 in relation to 1000 W/m^2, 25 °C, AM 1.5.

Maximum system voltage	:	500	V

The data in this document conforms to the DIN 40025 standard.

Typical I/V characteristics

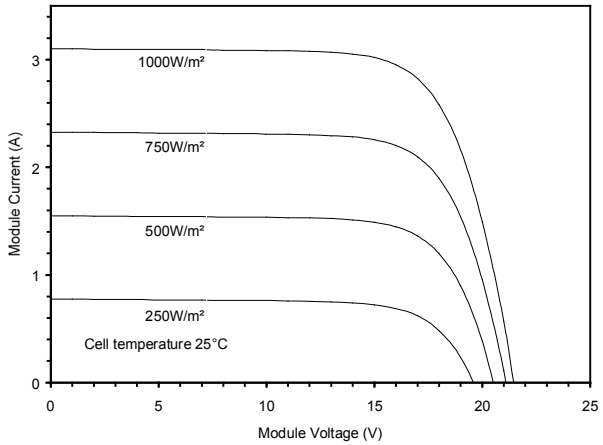

The I/V characteristic above shows the typical performance of the solar module at various levels of irradiance.

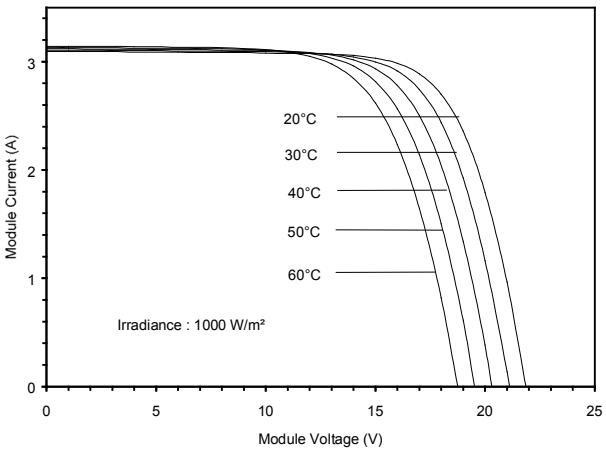

The I/V characteristic above shows the typical performance of the solar module at various cell temperatures.

Authorised Distributor:

Mounting example of solar module

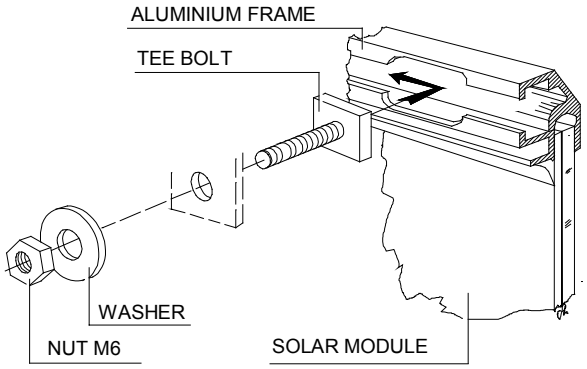

The drawing above shows how the tee bolts are to be inserted inside the module frame.
The maximum torque for the tee bolts is 9.0 Nm.

For detailed information about installation and wiring refer to the general installation instructions: DSO 027.

ELECTRICAL EQUIPMENT,
CHECK WITH YOUR INSTALLER,

Shell Solar

Product Information Sheet

Shell SM55 Photovoltaic Solar Module

General

The Shell SM55 module contains 36 series connected 103 x103 mm PowerMax® mono-crystalline silicon solar cells.

The Shell SM55 can generate a peak power of 55 watts at 17.4 volts.

The Shell SM55 solar module has been designed for rural and industrial applications.

Qualifications and Certificates

The Shell SM55 solar module meets the following requirements:

- **IEC 61215**
- **UL - Listing 1703**
- **TÜV Isolation Class II**

All Shell Solar modules are produced in EN-ISO 9001 certified factories.

Limited Warranties

- **Peak Power for 25 years**

Shell SM55 Module

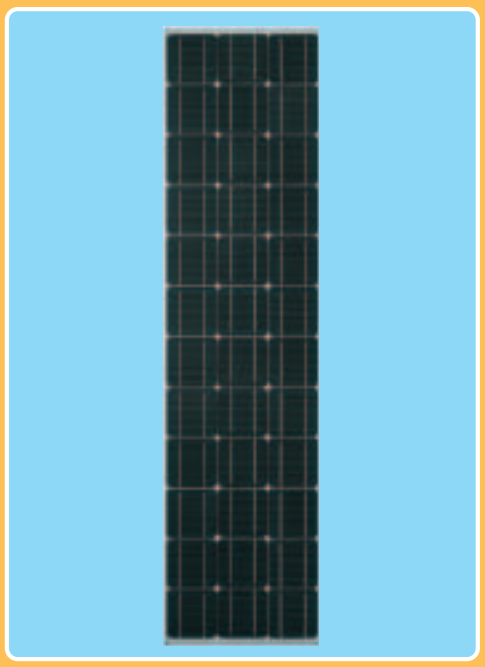

Junction Box

The junction box provides a high quality, dust protected and splash proof IP44-rated housing. The housing contains a rigid connection block with screw terminals and by-pass diodes providing "hot spot" protection for the solar cells.

ProCharger™-S Junction-Box

Maximum conductor cross-section: 4 mm²

Type of protection: IP44

Number of by-pass diodes: 2

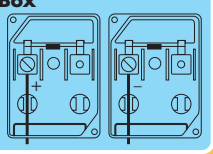

Benefits

- **PowerMax® mono-crystalline solar cells deliver maximum power output even under reduced light conditions providing more power where space is a limitation.**
- **The surface of the PowerMax® cell has a pyramidal textured surface to enable more light absorption and deliver exceptional efficiency.**
- **Highly transparent tempered glass delivers more power and ensures high impact resistance and protection against hail, snow, ice, and storms.**
- **Nearly 300MW of cumulative installed experience has been applied to the evolution of our mono-crystalline range to ensure that our products have a long and reliable service life backed by a 25 year warranty.**

ELECTRICAL EQUIPMENT, CHECK WITH YOUR INSTALLER

Shell SM55 Photovoltaic Solar Module

Mechanical Specifications Module

A torsion and corrosion-resistant anodized aluminium frame ensures dependable performance, even under harsh weather conditions. Pre-drilled mounting holes are provided for ease of installation.

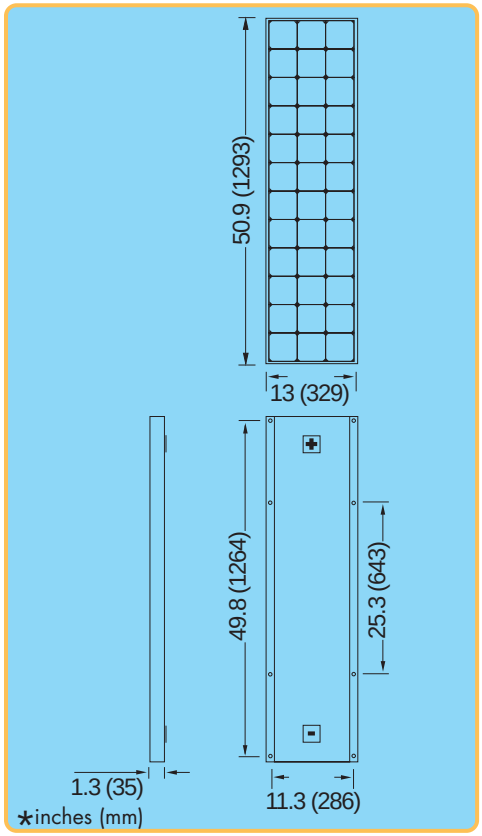

Outside dimensions (in)	50.9 x 13
Thickness (inc. junction box) (in)	1.3
Thickness (exc. junction box) (in)	1.3
Weight (lbs)	12

For installation instructions, please refer to the **Installation Manual** which is available from Shell Solar.

Electrical Characteristics

Data at Standard Test Conditions (STC)

STC: irradiance level 1000W/m^2, spectrum AM 1.5 and cell temperature 25°C

Rated power	P_r	55W
Peak power	P_{mpp}	55W
Peak power voltage	V_{mpp}	17.4V
Peak power current	I_{mpp}	3.15A
Open circuit voltage	V_{oc}	21.7V
Short circuit current	I_{sc}	3.45A
Series fuse rating		10A
Minimum peak power	$P_{mpp\ min}$	50W

The abbreviation 'mpp' stands for Maximum Power Point.

Typical data at Nominal Operating Cell Temperature (NOCT) conditions

NOCT: 800W/m^2 irradiance level, AM 1.5 spectrum, wind velocity 1m/s, T_{amb} 20°C

Temperature	T_{NOCT}	45°C
Mpp power	P_{mpp}	40W
Mpp voltage	V_{mpp}	15.9V
Open circuit voltage	V_{oc}	19.9V
Short circuit current	I_{sc}	2.8A

Typical data at low irradiance

The relative reduction of module efficiency at an irradiance of 200W/m^2 in relation to 1000W/m^2 both at 25°C cell temperature and AM 1.5 spectrum is 7%.

Temperature coefficients

$\alpha\ P_{mpp}$	–0.45 %/°C
$\alpha\ V_{mpp}$	–76 mV/°C
$\alpha\ I_{sc}$	+1.4 mA/°C
$\alpha\ V_{oc}$	–76 mV/°C

Maximum system voltage: 600 Vdc

Typical I/V Characteristics

The I/V graph below shows the typical performance of the solar module at various levels of irradiance.

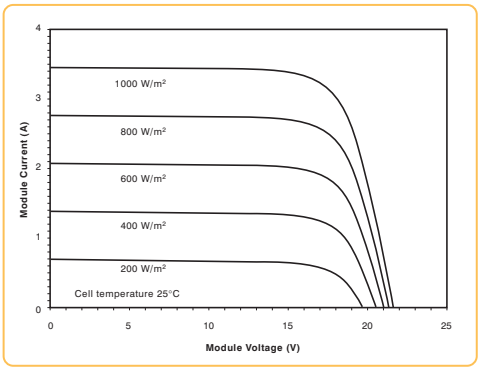

The I/V graph below shows the typical performance of the solar module at various cell temperatures.

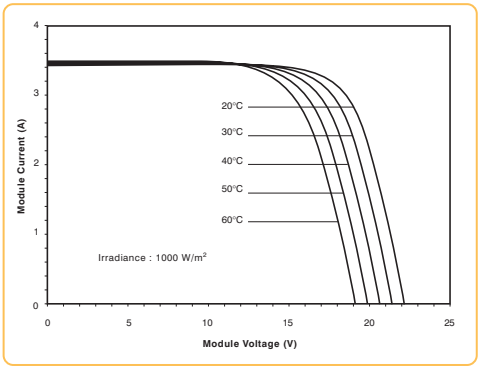

References in this Product Information Sheet to 'Shell Solar' are to companies and other organizational entities within the Royal Dutch/Shell Group of Companies that are engaged in the photovoltaic solar energy business. Shell Solar was set up in 1999 and has its principal office in Amsterdam, the Netherlands.

For further information on all Shell Solar products contact:

Shell Solar
4650 Adohr Lane, Camarillo CA 93012
805•482•6800 Fax 805•388•6511
Web www.shell.com/renewables

V2/SM55/05/02/US

Shell Solar

Product Information Sheet

Shell ST40 Photovoltaic Solar Module

General

The Shell ST40 module is composed of a monolithic structure of series connected Copper Indium Diselenide (CIS) based solar cells.

The Shell ST40 can generate a peak power of 40 watts at 16.6 volts.

The Shell ST40 solar module has been designed for grid connected applications.

Qualifications and Certificates

The Shell ST40 solar module meets the following requirements:

- **UL – Listing 1703**

All Shell Solar modules are produced in EN-ISO 9001 certified factories.

Limited Warranties

- **Peak Power for 10 years**

Shell ST40 Module

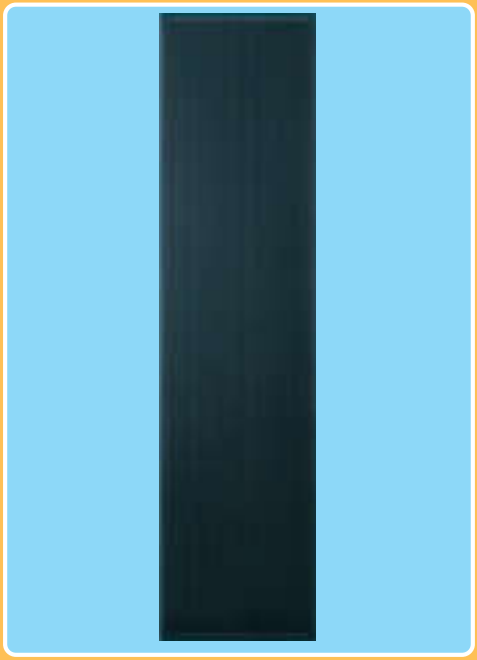

Junction Box

The junction box provides a high quality, dust protected and splash proof IP44-rated housing. The housing contains a rigid connection block with screw terminals and by-pass diodes providing "hot spot" protection for the solar cells.

ProCharger™–S Junction Box

Maximum conductor cross-section: 4 mm²

Type of protection: IP44

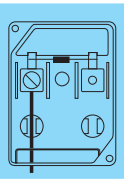

Benefits

- **Exceptional performance under low light conditions, shade and high temperature tolerance that offers reliable power in adverse or changeable conditions.**
- **Class leading efficiency and stable output power delivering reliable high performance for many years.**
- **Highly transparent tempered glass delivering more power and ensuring high impact resistance and protection against hail, snow, ice, and storms.**
- **Uniform appearance ideal for applications where aesthetics are an important factor.**
- **10 years research and over 3 years commercial manufacturing experience has been applied to the development of our CIS thin-film range to ensure that our products have a long and reliable service life backed by a 10 year warranty.**

ELECTRICAL EQUIPMENT, CHECK WITH YOUR INSTALLER

Due to continuous research and product improvement the specifications in this Product Information Sheet are subject to change without notice. Specifications can vary slightly. For installation and operation instructions, see the applicable manuals. No rights can be derived from this Product Information Sheet and Shell Solar assumes no liability whatsoever connected to or resulting from the use of any information contained herein.

Shell ST40 Photovoltaic Solar Module

Mechanical Specifications Module

A torsion and corrosion-resistant anodized aluminium frame ensures dependable performance, even under harsh weather conditions. Pre-drilled mounting holes are provided for ease of installation.

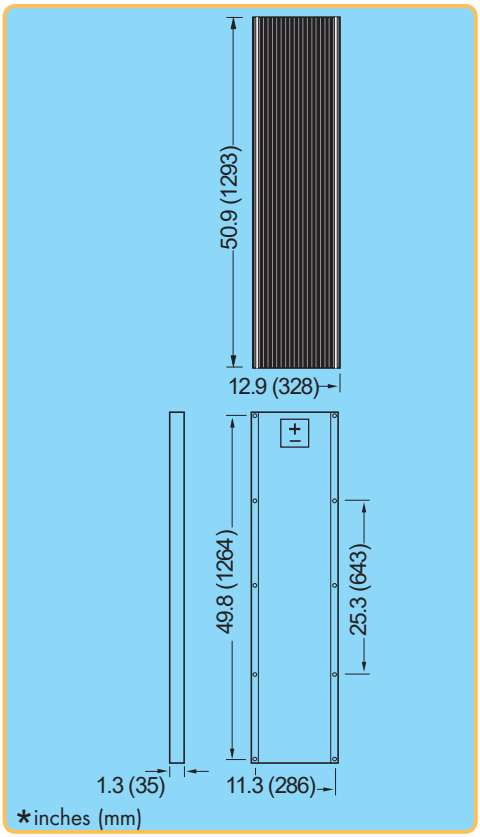

Outside dimensions (in)	50.9 x 12.9
Thickness (inc. junction box) (in)	1.3
Thickness (exc. junction box) (in)	1.3
Weight (lbs)	15.4

For installation instructions, please refer to the **Installation Manual** which is available from Shell Solar.

Electrical Characteristics

Data at Standard Test Conditions (STC)

STC: irradiance level 1000W/m^2, spectrum AM 1.5 and cell temperature 25°C

Rated power	P_r	40W
Peak power	P_{mpp}	40W
Peak power voltage	V_{mpp}	16.6V
Peak power current	I_{mpp}	2.41A
Open circuit voltage	V_{oc}	23.3V
Short circuit current	I_{sc}	2.68A
Series fuse rating		5A
Minimum peak power	$P_{mpp\ min}$	36W

The abbreviation 'mpp' stands for Maximum Power Point.

Typical data at Nominal Operating Cell Temperature (NOCT) conditions

NOCT: 800W/m^2 irradiance level, AM 1.5 spectrum, wind velocity 1m/s, T_{amb} 20°C

Temperature	T_{NOCT}	47°C
Mpp power	P_{mpp}	27.7W
Mpp voltage	V_{mpp}	14.7V
Open circuit voltage	V_{oc}	20.7V
Short circuit current	I_{sc}	2.2A

Typical data at low irradiance

The relative reduction of module efficiency at an irradiance of 200W/m^2 in relation to 1000W/m^2 both at 25°C cell temperature and AM 1.5 spectrum is 5%.

Temperature coefficients

αP_{mpp}	–0.6 %/°C
αV_{mpp}	–100 mV/°C
αI_{sc}	+0.35 mA/°C
αV_{oc}	–100 mV/°C

Maximum system voltage: 600 Vdc

Typical I/V Characteristics

The I/V graph below shows the typical performance of the solar module at various levels of irradiance.

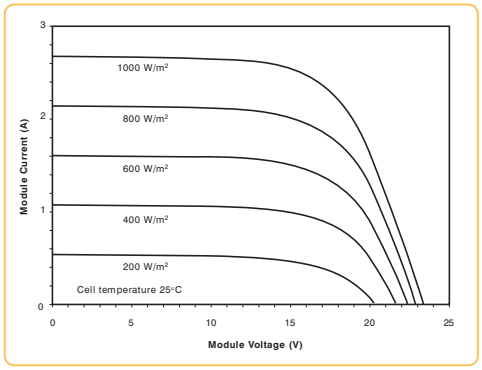

The I/V graph below shows the typical performance of the solar module at various cell temperatures.

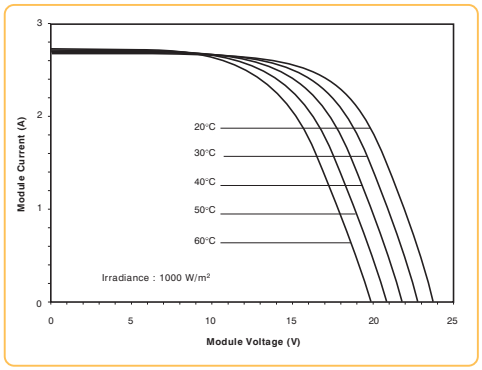

References in this Product Information Sheet to 'Shell Solar' are to companies and other organizational entities within the Royal Dutch/Shell Group of Companies that are engaged in the photovoltaic solar energy business. Shell Solar was set up in 1999 and has its principal office in Amsterdam, the Netherlands.

For further information on all Shell Solar products contact:

Shell Solar
4650 Adohr Lane, Camarillo CA 93012
805•482•6800 Fax 805•388•6511
Web www.shell.com/renewables

V2/ST40/05/02/US